

SENTINEL-3 OPTICAL PRODUCTS AND ALGORITHM DEFINITION

SYN Algorithm Theoretical Basis Document

DOCUMENT REF: S3-L2-SD-03-S02-ATBD

DELIVERABLE REF: SD-03-S2

VERSION: 2.5

CREATION DATE: 2009-06-22

LAST MODIFIED: 2017-08-03

	Name	Function	Company	Signature	Date
Prepared	P. North,	Reader	Swansea University		03.08.2017
	A. Heckel,	Researcher	Swansea University		03.08.2017
Approved					
Released					

DOCUMENT CHANGE RECORD

VERSION	DATE	DESCRIPTION	APPROVED
1.0	2009-06-22	Initial version	
2.0	2009-08-30	Major revision	
2.1	2009-10-29	Minor revision	
2.2	2010-06-30	Major revision	
2.3	2010-07-08	Minor revision	
2.4	2012-09-24	Minor revision	
2.5	2017-08-03	Revision – remove absorbing bands in retrieval	

FROM 2.1 TO 2.2

PAGE	SECTION	COMMENTS
10	1.5+ following	Document restructured to discuss radiative transfer modelling, aerosol retrieval and atmospheric correction before VGT simulation
20	4.3	Description of colocation
21	4.4	Discussion of cloud screening
21-26	4.5	Revised parameterisation of atmospheric LUTs and treatment of gaseous absorption
29	4.7	Clarification of determination of weight vector for eq (11)
32-33	4.8	Error estimates for AOT and surface reflectance
33	4.9	Description of interpolation of aerosol field for atmospheric correction
35	4.10	Product description added to include uncertainties and flags
42	5.1	Discussion of sensitivity to missing sensor data
46-50	6.1-6.2	Major revision of VGT spectral band mapping method to follow VGT study closely, interpolating on surface reflectance prior to propagation to TOA

6.2.2	51	LUT description for VGT simulation studies
6.2.3	51-53	Added description of formation of P product, including flags and reprojection

FROM 2.2 TO 2.3

PAGE	SECTION	COMMENTS
Various	-	Correction of minor typographical errors

FROM 2.3 TO 2.4

PAGE	SECTION	COMMENTS
22-25	4.5	Change in LUT transmittance file (p24) to include downwards and upwards zenith angles, and corresponding change in equations (1) on p22 and (7) on p25.
34	4.9.1	Included description of algorithm for interpolation of aerosol properties corresponding to RBD

FROM 2.4 TO 2.5

PAGE	SECTION	COMMENTS
20-25	4.24.5	Specification of retrieval algorithm to extend exclusion of absorption channels, to exclude S3 channel S4, and OLCI channels Oa13-15 and Oa19-20. Table 5 inserted (p22).
31	4.7.1	Clarification of channel weighting excluding absorbing channels.

Table of Contents

1	INTRODUCTION	8
1.1	Purpose and Scope	8
1.2	Applicable Documents	8
1.3	Reference Documents	9
1.4	Acronyms.....	9
1.5	Organisation of the document	10
2	ALGORITHM OVERVIEW	12
2.1	Objectives.....	12
2.2	Products	12
3	INSTRUMENT CHARACTERISTICS.....	13
3.1	Sentinel-3 OLCI and SLSTR.....	15
3.1.1	<i>Ocean and Land Colour Instrument (OLCI)</i>	15
3.1.2	<i>Sea and Land Surface Temperature Radiometer (SLSTR)</i>	15
3.2	SPOT VEGETATION	15
4	ALGORITHM DESCRIPTION – ATMOSPHERIC CORRECTON	16
4.1	Theoretical Description	16
4.1.1	<i>Atmospheric correction</i>	16
4.1.2	<i>Aerosol optical depth and scattering models</i>	17
4.1.3	<i>Existing single-instrument algorithms</i>	17
4.1.4	<i>Instrument synergy</i>	20
4.2	Algorithm outline	20
4.3	Collocation	22
4.4	Cloud Screening.....	22
4.5	Derivation of surface reflectance	22
4.5.1	<i>Approximation of atmospheric radiative transfer</i>	23
4.5.2	<i>Ozone correction</i>	23
4.5.3	<i>Aerosol model database</i>	24
4.5.4	<i>LUT approximation of RT coefficients</i>	24
4.5.5	<i>Estimation of surface reflectance</i>	26
4.6	Constraints on surface reflectance.....	28
4.6.1	<i>Dark object constraint</i>	28
4.6.2	<i>Multiple View-Angle (MVA) constraint</i>	29
4.7	Numerical inversion	31
4.7.1	<i>AOD retrieval</i>	31
4.7.2	<i>Selection of optimal aerosol model</i>	32
4.8	Retrieval error estimate	34

4.8.1	<i>Error in AOD</i>	34
4.8.2	<i>Surface reflectance error</i>	34
4.9	Atmospheric correction over land.....	35
4.9.1	<i>Aerosol Parameter Interpolation (API)</i>	35
4.10	Summary of products.....	38
4.11	Accuracy assessment.....	39
4.11.1	<i>Test sites and instrument co-location</i>	39
4.11.2	<i>Evaluation on satellite imagery</i>	40
4.11.2	<i>Evaluation of aerosol model retrieval</i>	44
4.11.3	<i>Comparison with AERONET stations</i>	44
4.11.4	<i>Sensitivity to missing sensor data</i>	45
4.12	Summary	47
4.12.1	<i>Assumptions and limitations</i>	47
5	ALGORITHM DESCRIPTION – VGT CONTINUITY	48
5.1	Theoretical Description	48
5.2	Algorithm implementation.....	48
5.2.1	<i>Overview</i>	48
5.2.2	<i>Spectral band mapping procedure</i>	50
5.2.3	<i>TOA Processing (VGT P)</i>	52
5.2.4	<i>S1 and S10 Products</i>	55
5.3	Assumptions and limitations	56
6	CONCLUSIONS	57
7	REFERENCES	57

List of Figures

Figure 1. Outline processing algorithm for synergistic retrieval.....	21
Figure 2: Relation of TOA to surface reflectance by lookup table	26
Figure 3. Plots for Tomsk showing retrieval for a range of possible aerosol models.	33
Figure 4. Tomsk site (15/5/2003) showing interpolation and atmospheric correction.....	37
Figure 5. Location of image sets selected for aerosol retrieval validation.	39
Figure 6. Results of Synergy Retrieval over Lille site, 14/7/2003.	42
Figure 7. Results of Synergy Retrieval over Ouagadougou site, 6/2/2003.	42
Figure 8. Results of Synergy Retrieval over Abracos Hill site, 31/7/2005.....	43
Figure 10. Plots for Beijing (12/10/2006) showing retrieval for a range of possible aerosol models..	44
Figure 11. Results of Synergy retrieval compared with AERONET sites (DDV targets only).	46
Figure 12. Results of Synergy Retrieval compared with AERONET (full data set),.....	46
Figure 13. Overview of SPOT-VGT product simulation.....	45
Figure 14. Overview of SPOT-VGT spectral band mapping procedure.....	48
Figure 15: VGT 1 km Plate-Carrée grid cell (green square).....	55

List of Tables

Table 1: Applicable documents	8
Table 2: Reference documents	9
Table 3: OLCI, SLSTR and VGT instrument characteristics.	13
Table 4: Channels on the SLSTR, OLCI AND VGT instruments.....	14
Table 5: Absorption channels not used in processing for SLSTR and OLCI.	22
Table 6: Sun-sensor geometry used in the LUT for SLSTR, OLCI.	27
Table 7: Parameters used in LUT for all instruments.....	27
Table 8: Aerosol types calculated from external mixtures from 6 basic components	28
Table 9. Test site location and cover type	40
Table 10: VEGETATION spectral band specifications and Sentinel-3 bands required for simulation ..	50
Table 11: Breakpoints used in the LUT for VGT TOA hyperspectral simulation.	52
Table 12: VGT P product pixel data	53
Table 13: VGT S product pixel data.....	53
Table 14: VGT status flags.....	54

1 INTRODUCTION

1.1 Purpose and Scope

This document describes the algorithms for synergistic processing of data from SLSTR and OLCI to (i) retrieve aerosol optical properties and surface reflectance for cloud-free atmospheres over land, and (ii) to provide comparable products to SPOT-VGT, to allow continuity of data delivery for existing user community of SPOT-VGT. The document includes all assumptions, discusses technical tradeoffs and describes the algorithms in terms of physical background as well as mathematical breakdown.

1.2 Applicable Documents

This document is in compliance with the applicable documents listed in Table 1.

Table 1: Applicable documents

Ref	Title	Document Code	Version	Date
AD-1	GMES Sentinel-2 and Sentinel-3 Products and Algorithms Definition	GMES-DFPR-EOPG-SW-07-0008	1.11	2007-09-12
AD-2	Sentinel-3 Mission Requirements Document	EOP-SM/1151/MD-md	2.0	2007-02-19
AD-3	GMES Sentinel-3 System Requirements Document	S3-RS-ESA-SY-0010	3.0	2007-10-17
AD-4	GMESPH Guidelines for Sentinel-3 Products Definition	GMESPH-DME-TEC-TNO09-E	2.0	2008-08-01
AD-5	ECSS Space Engineering Software – Part 1: Principles and requirements	ECSS-E-40 Part 1B		2003-11-28
AD-6	ECSS Space Engineering Software – Part 2: Document Requirements Definitions	ECSS-E-40B Part 2B		2005-03-31

1.3 Reference Documents

The reference documents taken into account in preparing this document are listed in Table 2.

Table 2: Reference documents

Ref	Title	Document Code	Version	Date
RD-1	Sentinel-3 L2 Products and Algorithm Definition: SYN Product Definition	S3-L2-SD-05-S-BC-PD	2.1	2010-05-06
RD-2	Sentinel-3 Level 0, Level 1 Products Definition - Part 2: Optical Products – Volume 4: Level 1c Product	S3-RS-TAF-SY-01247	2.0	2010-02-01
RD-3	Sentinel-3 OLCI Level 2 Algorithm Theoretical Basis Document Pixel Classification	S3-L2-SD-03-C01-LISE-ATBD	2.0	2010-04-08
RD-4	Sentinel-3 L2 Products and Algorithm Definition: SYN IODD	S3-L2-SD-08-S-BC-IODD	2.1	2010-05-06
RD-5	Sentinel-3 Land Synergy Products for SPOT VGT Continuity, Final Report of ESA Study NO. 20867 /07/NL/CB	TAP/N7944-S3VGT/PK/FR	1.5	2008-09-11
RD-6	Sentinel-3 Land Synergy Products for SPOT VGT Continuity, ATBD for spectral band mapping, ESA Study NO. 20867 /07/NL/CB	S3-L1VGT-ATBD	1.2	2009-04-30
RD-7	Sentinel-3 Land Synergy Products for SPOT VGT Continuity, Technical Note 2: Key VGT Product Processing Chain Element Requirements	TAP/N7944-S3VGT/PK/07-04	1.3	2007-12-07

1.4 Acronyms

AATSR	Advanced Along Track Scanning Radiometer
AOD	Aerosol Optical Depth
BEAM	Basic Envisat AATSR and MERIS
BRDF	Bi-directional Reflectance Distribution Function
BRF	Bi-directional Reflectance Factor
DOM	Dark Object Methods
FR	Full Resolution

FLIGHT	Forest Light Radiative transfer Model
GMES	Global Monitoring for Environment and Security
LAI	Leaf Area Index
LUT	Look-up table
MERIS	Medium Resolution Imaging Spectrometer
MODIS	Moderate Resolution Imaging Spectrometer
MOMO	Matrix Operator Model
NDVI	Normalised Differential Vegetation Index
NIR	Near Infrared
OLCI	Ocean and Land Colour Instrument
PTD	Product Tree Definition
RAZ	Relative Azimuth Angle
RR	Reduced Resolution
S1	VEGETATION daily synthesis (maximum NDVI composite)
S10	VEGETATION decade synthesis (10-day maximum NDVI composite)
S-3, S3	Sentinel-3
SDR	Surface Directional Reflectance
SLSTR	Sea and Land Surface Temperature Radiometer
SWIR	Shortwave Infrared
SZA	Solar Zenith Angle
TIR	Thermal Infrared
TOA	Top of Atmosphere
TOC	Top of Canopy
VGT	VEGETATION (sensor) onboard the SPOT satellite
VZA	View Zenith Angle

1.5 Organisation of the document

The document is divided into the following sections:

Section 1: Introduction gives the scope, purpose, reference and applicable documents, and list of acronyms

Section 2: Algorithm overview gives a summary of the objectives of the processing, and a list of products from VGT continuity, atmospheric correction, and a list of potential further synergy products for consideration.

Section 3: The characteristics of the SLSTR, OLCI and SPOT VEGETATION instruments are summarised.

Section 4: The algorithm to estimate aerosol and surface reflectance from TOA OLCI and SLSTR synergy is presented. The main components of this algorithm are (i) radiative transfer modelling of TOA reflectance to generate lookup tables for a range of aerosol optical depths and aerosol model types (ii) definition of parameterised models of land surface spectral and angular reflectance, (iii) an inversion algorithm to estimate the optimal atmospheric profile, and (iv) atmospheric correction to estimate surface reflectance for SLSTR and OLCI channels.

Section 5: An outline of the algorithm for VGT continuity products is given, listing main processing steps for generation of equivalent P, S1 and S10 products from SLSTR/OLCI synergy.

Section 6: Conclusions on the use of synergy from Sentinel-3 instruments are given, and an outline of further research recommended.

2 ALGORITHM OVERVIEW

2.1 Objectives

The objectives are to define algorithms making use of the combined information from the OLCI and SLSTR instruments on Sentinel-3 to provide improved data for land surface analysis. There are two strands to the processing. The first makes use of the enhanced spectral and angular capabilities of a combined instrument to propose a product with atmospherically corrected surface reflectance, and corresponding information on aerosol properties. The second is to allow processing of data from SLSTR and OLCI to provide comparable products to SPOT-VGT, to allow continuity of data delivery for existing user community of SPOT-VGT.

2.2 Products

Two sets of products are defined in this ATBD, firstly for surface reflectance and aerosol, and secondly for VGT continuity and [RD-1]. All algorithms assume as input Sentinel-3 L1C data, which have been mapped to a common grid [RD-2]. Although not discussed further in this document, consideration has been given to further products which exploit the synergistic information from the two instruments, where some preliminary research has taken place, and are recommended for additional products if research reaches maturity.

1. Land Surface Reflectance and Aerosol Products

- Atmospherically corrected SDR at all STSTR and OLCI wavebands, other than within gaseous absorption bands (O_2 , H_2O), R_i
- AOD at reference waveband (550nm) τ_{550}
- Angstrom coefficient α
- Aerosol model index number M_a
- Error estimate (1 s.d.) in AOD $\Delta\tau_{550}$
- Error estimate (1 s.d.) in surface reflectance at each waveband
- Error flag to indicate high uncertainty in retrieval / interpolation of AOD used

2. SPOT VEGETATION Continuity Products

- P Product (simulated TOA reflectance)
- S1 product: daily synthesis (maximum NDVI composite)
- S10 Product: decade synthesis (10-day maximum NDVI composite)

3. Potential Further Synergy Products:

- Improved cloud mask
- Ocean aerosol
- Snow mask
- Vegetation index
- Fraction of absorbed photosynthetically active radiation (fAPAR)
- Ice flag
- Land / water classification

3 INSTRUMENT CHARACTERISTICS

This section outlines the principal characteristics of the Sentinel-3 optical instruments, SLSTR and OLCI (Aguirre et al., 2007), and the SPOT-VEGETATION instrument (Saint, 1994). The instrument characteristics and channels are presented in Tables 3 and 4 respectively. A pre-requisite for synergy is that the images attained by the dual instrument combination need to be co-registered.

Table 3: OLCI, SLSTR and VGT instrument characteristics.

Instrument	OLCI	SLSTR	VGT
Bands	Up to 21 between 0.4 and 1.0 μm	9 channels (AATSR + 1.3 and 2.2 μm)	4
Swath Width	1269 km	1420 km nadir, 750 km off-nadir	~2250 km
Spatial Resolution	~300m	~500 m	1.15km
Range of view zenith angles	0-55°	Oblique: 55° Nadir: 6-60°	0-55°

Table 4: Channels on the SLSTR, OLCI AND VGT instruments.

OLCI			SLSTR			VGT		
Channel	Wave-length (nm)	Band-width (nm)	Channel	Wave-length (nm)	Band-width (nm)	Channel	Wave-length (nm)	Band-width (nm)
1	400	15						
2	412.5	10						
3	442.5	10				1	450	40
4	490	10						
5	510	10						
6	560	10	1	550	20			
7	620	10						
8	665	10	2	665	20	2	645	70
9	673.75	7.5						
10	681.25	7.5						
11	708.75	10						
12	753.75	7.5						
13	761.25	2.5						
14	764.37	3.75						
15	767.5	2.5						
16	778.75	15	3	865	20	3	850	110
17	865	20						
18	885	10						
19	900	10						
20	940	20						
21	1020	40						
			4	1375	15			
			5	1610	60	4	1660	195
			6	2250	50			
			7	3740	380			
			8	10850	90			
			9	12000	1000			

3.1 Sentinel-3 OLCI and SLSTR

The ESA contribution to the Global Monitoring for Environment and Security (GMES) will include the Sentinel series of operational satellites. Sentinel-3 is dedicated land and ocean applications including sea-ice and coastal zones monitoring. The system consists of a series of 5 satellites performing continuous and systematic acquisitions for 20 years, and the associated ground segment. Each satellite is designed with a 7-year lifetime, with the first satellite scheduled for launch in 2012. The mission requirements will be met by pair of satellites simultaneously in-orbit with 180° dephasing. The satellite will have sun-synchronous orbit with 14+7/27 revolutions per day with a mean altitude of 815 km and a local equatorial crossing time of 10:00 a.m. Each satellite will consist of two optical instruments, OLCI and SLSTR, and the topography payload that includes a synthetic aperture radar altimeter (SRAL) for measuring sea surface height. The SLSTR and OLCI instruments on-board Sentinel-3 will provide continuity to the AATSR and MERIS sensors, respectively.

3.1.1 Ocean and Land Colour Instrument (OLCI)

The OLCI (Ocean and Land Colour Instrument) is based on Envisat MERIS but with a larger swath width of 1269km compared with MERIS' swath width of 1150km. In addition, improved revisit performances will be due to an eastward pointing field-of-view away from the sun in order to reduce ocean sun-glint. The revisit is less than 2 days for ocean colour observations compared with 15 days for ENVISAT/MERIS. The OLCI instrument will have the same spectral characteristics as MERIS but with an additional 6 bands in the visible and NIR region optimised for improved atmospheric correction. It will also consist of 5 cameras so that the problems of spectral calibration within each camera and from camera to camera will be similar to those of MERIS.

3.1.2 Sea and Land Surface Temperature Radiometer (SLSTR)

The Sea and Land Surface Temperature Radiometer (SLSTR), is based on AATSR but with an extended swath width in nadir view of 1420 km to fully cover the OLCI swath and a 750km swath in the off-nadir view. However, there are some important differences between AATSR and SLSTR, most notably the inclusion of an additional two channels at 1.3 and 2.2 microns and reconfiguration of the off-nadir observation to point in the backward direction instead of forward. In addition, SLSTR will have a nominal spatial resolution of 500m.

3.2 SPOT VEGETATION

The first SPOT VGT sensor was launched on SPOT4 in 1998, and succeeded by VGT2, on SPOT5 in 2002. By 2010-2012, the VEGETATION instruments will have reached the end of their operating lifetime, and it is intended to allow continuity of some VEGETATION products by ESA's GMES Sentinel-3. The instrument has a wide swath width, allowing near-daily collection of global data, at a spatial resolution of ~1.15 km. Relative to SLSTR and OLCI there are a small number of bands (4), but spanning a wide spectral range. Characteristics are summarised in Tables 3 and 4.

4 ALGORITHM DESCRIPTION – ATMOSPHERIC CORRECTON

4.1 Theoretical Description

Atmospherically corrected surface reflectances allow quantitative analysis of the surface, such as the retrieval of LAI (leaf area index), fAPAR (fraction of absorbed photosynthetically active radiation) and other biophysical properties (North 2002a; Prieto-Blanco et al., 2009). While the effects of aerosols and absorbing gases may be modelled, the variability of aerosol scattering typically represents the greatest uncertainty in derivation of surface reflectance over land and ocean from remotely-sensed data. Atmospheric aerosols also represent one of the greatest uncertainties in our understanding of the climate system (Solomon et al., 2007; Bellouin et al., 2005). This is principally due to a lack of accurate and repetitive measurements at global scales, in particular over the land surface where it is difficult to separate surface scattering from the atmospheric signal. Aerosols influence climate change through their direct radiative forcing and link with cloud formation, their influence on the directionality of the surface downwelling radiation and their possible feedbacks with rainfall (Twomey 1974; Rosenfeld et al., 2001; Alton et al., 2007).

4.1.1 Atmospheric correction

Satellite datasets need to be processed from top-of-atmosphere (TOA) observations to obtain surface spectral bi-directional reflectance factors (BRF), also termed surface directional reflectance (SDR). The initial satellite measurements are strongly affected by molecular and aerosol scattering, and absorption by ozone and water vapour. While vicarious correction techniques, such as the empirical line method, have been applied to individual sites as an extension of calibration, this requires *in situ* measurement of sample surface reflectance.

For global satellite data processing, atmospheric correction is normally performed in two stages. In the first step, the atmospheric properties are determined at the time of satellite overpass. Secondly, a radiative transfer model of the atmosphere is inverted to estimate surface reflectance, accounting for the atmospheric scattering and absorption. It is normal to use a pre-calculated look-up table (LUT) for this stage, to allow rapid estimation of surface reflectance on a per-pixel basis (Rahman and Dedieu, 1994; Grey et al 2006a). Of these two stages, the estimation of atmospheric properties is the most challenging and greater source of error (Vermote and Kotchenova, 2008).

The high spatial and temporal variability of aerosol scattering typically represents the greatest uncertainty in derivation of surface reflectance over land. While climatology values for AOD have been used, for example in processing of SPOT VGT (Berthelot and Dedieu, 2000), derivation of aerosol properties from the satellite data at the time of overpass is needed for accurate correction. The parameters required to model aerosol radiative effects are AOD for a given reference wavelength, and aerosol model, describing spectral dependence of AOD, single scattering albedo, and phase function.

In general, it is more challenging to retrieve required aerosol properties over the land than the ocean. This is because the scattering from the land surface tends to dominate the satellite signal making it difficult to discern the atmospheric scattering contribution, particularly over bright surfaces. In addition, obtaining an accurate model of the land surface is further complicated because bi-directional reflectance is highly variable, both spatially and temporally.

Currently, atmospheric radiative transfer (RT) codes allow retrieval of surface reflectance with a high degree of precision for a known atmospheric profile, with theoretical error typically <0.01 in surface reflectance (Fischer and Grassl, 1984; Kotchenova et al., 2006). This enables both forward simulation of satellite radiances, and inversion of such models to estimate surface reflectance given a set of top-of-atmosphere (TOA) radiances. Over land, the key problem in correction of surface reflectance for aerosol effects lies in simultaneous estimation of aerosol at the time of acquisition.

4.1.2 Aerosol optical depth and scattering models

The parameters required to model aerosol radiative effects are aerosol optical depth (AOD) for a given reference wavelength, its spectral dependence, which may be defined by the Angstrom coefficient, single scattering albedo, and phase function. These properties are closely related to aerosol amount, composition and size distribution. The net effect of aerosol on climate forcing depends on its optical properties (absorption and scattering) (Mishchenko et al., 2007). To date, most retrieval schemes return spatially varying estimates of AOD as the main parameter, and some additionally return information on aerosol size distribution (e.g. Remer et al., 2005) or the related property of Angstrom coefficient (e.g. Veefkind et al 1999). Recent methods have explored search for the most probable candidate aerosol model from a limited database, based on fit to the observations, with further aerosol properties defined by this model (North 2002b; Holzer-Popp et al., 2008; Diner et al., 2009).

4.1.3 Existing single-instrument algorithms

4.1.3.1 Single-view methods

Most currently available aerosol retrievals are based on data from instruments with a single sampling of the angular domain. These algorithms are based on different assumptions, depending on available spectral sampling. In general the retrievals need to use known wavelength dependence of surface reflectance in order to provide information on the aerosol. The separation of the surface contribution is always based on a priori knowledge about the spectral properties of the surface. A number of assumptions have proven successful:

- Identification of dark targets: where it is possible to identify targets of dark dense vegetation (DDV) with known spectral properties, this may be used to derive aerosol path radiance over these targets (Kaufman and Sendra (1988)). Operational algorithms have been developed for MODIS (Remer et al., 2005), and MERIS (Santer et al., 1999; Santer et al., 2007) on this basis, amongst other instruments. For MERIS, the vegetation index ARVI (Kaufman et al., 1992) is used to identify vegetation. However, accurate application is limited to regions where such

targets are available at the appropriate spatial resolution (i.e. oceans and dark dense vegetation), so we must employ interpolation of the aerosol field to derive values at image points suitable for atmospheric correction. Recent results suggest improvement of this method is possible using calibration of the spectral relationship over a range of representative land covers, corresponding to selected AERONET sites (Levy et al., 2007) allowing correction for view-angle effects on surface spectra and generalisation to brighter surfaces (Hsu et al., 2004).

- Spectral mixing: Independently measured spectra of vegetation and bare soil are taken to construct a basis and the actual surface spectrum is assumed to be a linear combination of both, depending on vegetation cover. The algorithm described by von Hoyningen-Huene et al. (2003), bases the mixture of soil and vegetation spectra on the measured NDVI. The thus defined surface spectrum is then only allowed for scaling. An alternate algorithm developed by Guanter et al. (2007) uses mainly the assumption that aerosol is spatially more homogeneous than surface reflectance. Therefore the algorithm searches locally for pixels with the most and the least vegetation cover (darkest and brightest pixels) and assumes the atmospheric information to be constant. This allows the determination of the aerosol content.
- *A priori* assumptions based on existence of an independent estimate of surface reflectance from other instruments: For example Thomas et al. (2009) used MODIS estimates of surface reflectance to estimate aerosol from (A)ATSR instruments. While potentially allowing spatially continuous mapping of aerosol, important limitations are the reliance on the existence of a recent reflectance map from another instrument which has already been successfully corrected for atmospheric scattering, as well as including errors due to different temporal, angular and spectral sampling.

While potentially offering accurate retrieval where the target reflectance matches well with modelled spectrum, the single spectral measurement can give information on aerosol path radiance only, and not on phase function. Generally these methods, are suitable only for dark targets with relatively low spectral variability, so give a sparse estimate of optical depth, and are normally inappropriate for bright surfaces such as arid or snow covered land.

4.1.3.2 Multi-temporal methods

Related to single view retrieval methods are those which allow retrieval from time series, assuming greater stability of land surface reflectance compared to aerosol (Lyapustin, A. and Wang (2009)). The time series allows use of recent reflectance retrievals as a prior in inversion. Such techniques are particularly relevant where high temporal sampling is available, such as from geostationary instruments, for example the method by Govaerts et al., (2010) using optimal estimation theory and including a model of the effects of solar angle change on land surface scattering.

4.1.3.3 Multiple view-angle (MVA) methods

While spectral methods may produce very good results in regions where the assumptions are fulfilled, global aerosol retrievals show a number of uncertainties due to the large variability in spectral surface properties. Use of multiple view-angle imagery allows an additional constraint to be placed, since the same area of surface is viewed through different atmospheric path lengths. The concept was pioneered by ATSR on ERS-2, originally for atmospheric correction of SST for the effects of water vapour (Barton et al., 1989). In addition, there is scope to use the increased angular sampling of the land surface to further constrain retrieval of albedo and vegetation biophysical parameters (Diner et al., 1999). Several instruments have been designed to exploit the ability of MVA techniques for aerosol retrieval, including MISR, using 9 cameras tilted at angles in the range $\pm 70.5^\circ$ along-track, and POLDER, which employs a CCD array to sample continuously at $\pm 43^\circ$ along-track (Martonchik et al., 1998; Leroy et al., 1997).

For the ATSR instrument series, 2 view directions are available, at approximately nadir and 55° along-track requires an approach which exploits the similarity of the surface anisotropy across wavelengths. This is due to the fact the anisotropy is dominated by geometric shadowing effects, which are wavelength invariant. However other effects contribute to anisotropy; the differential viewing of canopy/understorey surfaces with view angle, and the degree of multiple scattering, which tends to reduce anisotropy over bright surfaces. A simple approximation assuming spectral invariance of the BRDF (Mackay et al., 1999; Flowerdew and Haigh, 1996). has been used in inversion schemes (Veefkind et al., 2000) to provide a successful retrieval of aerosol. The method has developed further to include enhanced modelling of the spectral variation of anisotropy (North et al., 1999) to give an operational method from which global retrieval of aerosol properties has been achieved using the ESA Grid Processing on Demand (GPOD) system (North 2002b; Grey et al., 2006a,b). Validation by comparison with AERONET shows robust retrieval over all land surfaces, including deserts (Grey et al., 2006b; Bevan et al., 2009). The method has also recently been applied to estimation of aerosol from the CHRIS PROBA instrument, by exploiting the ability of the instrument to acquire 5 views of the target by satellite pointing (Davies et al., 2010). The use of a cross-spectral constraint on surface anisotropy has also recently been incorporated into the MSR processing algorithm (Diner et al., 2005).

The principal advantage of an MVA approach is that no *a priori* information of the surface spectrum is required and aerosol properties can be retrieved over all surface types, including bright deserts. Limitations of the angular approach are that the algorithms require accurate co-registration of the images acquired from multiple view angles. Normally aerosol is retrieved at a lower resolution than the pixel resolution, to decrease the effect of misregistration errors, for example at 18km for MISR and 8km for ATSR (Diner et al., 2009; North et al., 2002b), and the methods may be sensitive to undetected sub-pixel clouds (North et al., 1999).

4.1.4 Instrument synergy

The principle of synergy is that combining information from multiple sources leads to greater benefit than considering in isolation. The potential for synergistic retrieval from satellite instruments has increasingly been recognised, both through simultaneous acquisition by mounting of instruments on the same platform, and through formation flying of instruments in the same orbit. For example, the *A-Train* concept was designed to give near-simultaneous measurement with multiple instruments over six satellites to allow potential for synergistic retrieval, and shows initial promising results for aerosol properties (Jeong and Hsu (2008)). A number of synergy methods have focused on deriving further information from the derived products of instruments, after single-instrument retrievals have taken place. This is particularly useful where complementary information is available, for example combining lidar height distribution with radar penetration (McGill et al., 2004). For aerosol retrieval, Holzer-Popp et al (1999) used ATSR-2 derived surface reflectance in subsequent retrieval of AOD from GOME, and SCHIAMACHY (Holzer-Popp et al., 1999; Holzer-Popp et al., 2008). Veefkind et al. (2000) explored improved characterization of Angstrom coefficient by combining AOD retrieved independently from ATSR-2 and GOME.

The approach in the proposed SLSTR/OLCI synergy algorithm is based on methods developed within the ESA MERIS/AATSR Synergy project. It aims to fully utilize synergy between SLSTR and OLCI to simultaneously retrieve parameters, based on a single inversion where information from a combined SLSTR/OLCI image is used as input as if from a single sensor.

4.2 Algorithm outline

The aim is to make use of the angular and spectral sampling available from SLSTR and OLCI to perform atmospheric correction and aerosol retrieval over land. The method takes as input TOA reflectance data for the SLSTR and OLCI, collocated to a common grid. While all channels are available for pre-processing, including cloud-screening and pixel classification, the retrieval of surface reflectance and aerosol uses only the non-absorbing channels (Table 5). The output therefore comprises reflectance at 5 solar reflective SLSTR bands at both nadir and forward views (a total of 10 channels), and the 16 OLCI bands at all non-absorbing channels (i.e. excluding OLCI oxygen bands 13-15 and water vapour bands 19-20). The output of aerosol gives optical depth at a standard reference waveband (550nm), an estimate of aerosol model and Angstrom coefficient, and atmospherically corrected surface reflectances for all bands used.

The problem is formulated as one of optimisation subject to multiple constraints, which has been widely applied to atmospheric retrievals (Dubovik 2005). Figure 1 illustrates the retrieval framework followed here. The two-stage optimization process is employed: (1) Given a set of satellite TOA radiances, and an initial guess of atmospheric profile, we estimate the corresponding set of surface reflectances. (2) Testing of this set against a constraint results in an error metric, where a low value of this metric should correspond to a set of surface reflectances (and hence atmospheric profile) which is realistic. Step (1) is repeated with a refined atmospheric profile until convergence at an optimal solution.

The algorithm components are therefore (i) design of an efficient and accurate scheme for deriving surface reflectance for known atmospheric profile, and (ii) formulation of constraints on the land surface reflectance suitable for SLSTR/OLCI synergy.

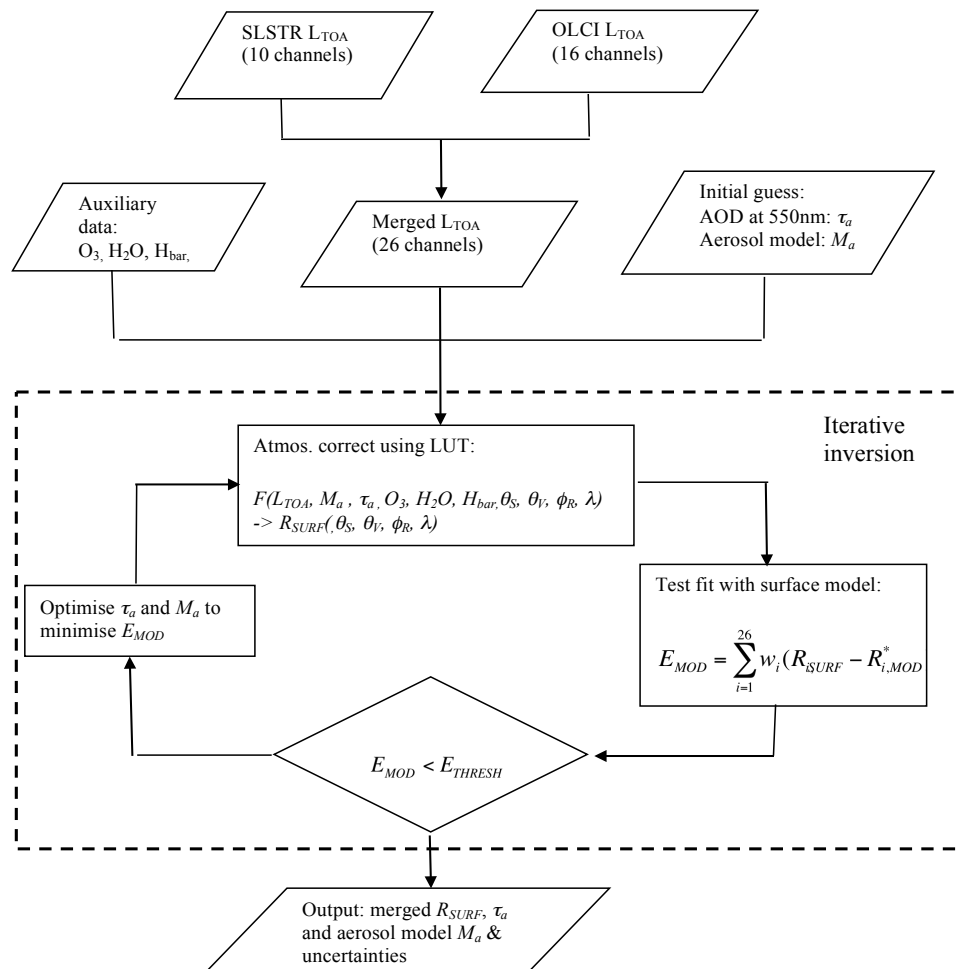


Figure 1. Outline processing algorithm for synergistic retrieval of surface reflectance (R_{SURF}) and aerosol properties (optical depth τ_a and aerosol model M_a) from merged SLSTR and OLCI data. The combined data allows atmospheric correction based on fit to a parameterised model of reflectance R_{MOD} .

4.3 Collocation

As a first stage in processing the L1c data is resampled to a single common grid. The input L1c product gives the geolocated pixel centre for both OLCI and SLSTR grids. We use the OLCI reference grid as a master, and resample the SLSTR data onto this grid, using nearest neighbour resampling. The reference grid is defined by the acquisition geometry of OLCI channel 17. The L1 product contains the TOA reflectance data for the 6 solar reflective SLSTR bands at both nadir and forward views (a total of 12 input channels), and the 21 OLCI bands. For the central 750km of the product we have the SLSTR along-track values. Tie point information for each band retains the original solar/view geometry of the OLCI/SLSTR sampling. The product includes all OLCI values, and all SLSTR where the swath overlaps with OLCI.

4.4 Cloud Screening

Cloud screening was not foreseen in the Statement of Work for the Sentinel-3 Optical Products and Algorithm Definition and therefore is not elaborated here. Instead we recommend a pragmatic approach using existing single-sensor flags, but may be sufficient for the purpose of sieving pixels, which are not suitable for retrieving aerosol parameters and surface reflectance:

1. For each pixel cloud flags are computed by logical OR combination of OLCI, SLSTR nadir and SLSTR along-track cloud flags in the collocated L1c. Cirrus clouds are flagged separately
2. For each pixel the L2 Pixel Classification algorithm [RD-3] over land is applied. The cloud flag is raised, if the pixel is not classified as surface (there is no atmospheric processing branch and so flags are driven by the possibility to retrieve the L2 land parameters).

The feasibility of using the L2 Pixel Classification algorithm [RD-3] over land is being evaluated.

4.5 Derivation of surface reflectance

Here we define a method to retrieve surface reflectance to retrieve surface reflectance for the combined SLSTR/OLCI images given known solar/view geometry and atmospheric constituents, based on approximation of an atmospheric radiative transfer model by lookup tables. For the derivation of surface reflectance, and use in simultaneous retrieval of atmospheric aerosol, only the non-absorbing bands of OLCI and SLSTR are used. The following bands are excluded from further processing:

Table 5: Absorption channels not used in processing for SLSTR and OLCI.

OLCI/SLSTR channel	Central Wavelength (nm)	Function (as described in S3 handbook)
Oa13	761.25	O2 absorption band
Oa14	764.375	Atmospheric Correction
Oa15	767.5	O2A used for cloud top pressure and fluorescence
Oa19	900	Water Vapour Absorption

Oa20	940	Water Vapour Absorption
S4	1.375	Cirrus detection over land

4.5.1 Approximation of atmospheric radiative transfer

Satellite observations at optical wavelengths consist of solar radiation scattered by both the atmosphere and the surface back in the direction of the sensor. We need to separate the atmospheric and surface scattering components through atmospheric radiative transfer modelling if we are to obtain accurate estimates of biophysical and geophysical properties. For remote sensing we are can infer the radiative characteristics of aerosol particles from the measured satellite radiances.

We note here that TOA radiances L_{TOA} can also be expressed as reflectances R_{TOA} using:

$$R_{TOA} = \frac{\pi L_{TOA}}{F_0 \cos(\theta_s)} \quad (1)$$

Where F_0 is exo-atmospheric solar irradiance. For a given sensor waveband, and atmospheric profile, the relationship between surface directional reflectance R_{surf} top of atmosphere reflectance R_{TOA} can be approximated by the equation:

$$R_{TOA}(\theta_v, \theta_s, \phi) = T_{O_3}(\theta_v, \theta_s) [R_{atm}(\theta_v, \theta_s, \phi) + T(\theta_v, \theta_s) \frac{R_{surf}(\theta_v, \theta_s, \phi)}{1 - \rho_{atm} R'_{surf}}] \quad (2)$$

where R_{atm} denotes the atmospheric scattering term (TOA reflectance for zero surface reflectance), T denotes atmospheric transmission for either sensor to ground or ground to sensor, and ρ_{atm} denotes atmospheric bi-hemispherical albedo. The term R'_{surf} denotes ground reflectance for multiple scattered light, and here we use the approximation $R'_{surf} = R_{surf}$. The term T_{O_3} denotes a separate correction factor for O_3 . All other atmospheric terms in (2) include the absorption and scattering of remaining fixed gases and water vapour. ECMWF fields are used for ozone, water vapour and surface pressure [RD-4].

Over a completely absorbing surface (e.g. over deep dark oceans at infrared wavelengths) the measured TOA radiance is due entirely to the atmospheric path radiance. In contrast, over bright land surfaces the surface reflectance term makes a large contribution to the measured TOA radiance.

4.5.2 Ozone correction

To calculate the term T_{O_3} , it is efficient to pre-compute a single correction factor $C_{O_3}(l)$ for each waveband (equivalent to effective absorption cross section across the whole waveband), which can be scaled by air mass & column ozone concentration in Dobson Units (DU).

The value C_{O_3} is defined for a given waveband by the equation

$$\ln(R_{TOA}/R_0) = -C_{O_3} * O_3 \text{ [DU] at SZA=0, VZA=0} \quad (3)$$

where reflectance R_{TOA} for an atmosphere containing O_3 is related to the reflectance R_0 equivalent atmosphere with zero O_3 , at nadir solar and viewing conditions. The value of C_{O_3} for each waveband is determined by radiative transfer simulation to calculate R_0 and R_{TOA} for a standard atmosphere at two levels of O_3 , at 0 and 400 DU respectively.

The geometric air mass factor M is defined as

$$M = 0.5 \left(\frac{1}{\cos(\theta_s)} + \frac{1}{\cos(\theta_v)} \right) \quad (4)$$

the transmission term T_{O_3} reflectance including ozone is calculated as:

$$T_{O_3}(\lambda) = \exp(-M * O_3 \text{ [DU]} * C_{O_3}(\lambda)) \quad (5)$$

4.5.3 Aerosol model database

A set of aerosol models are required to define the optical properties in the LUTs. These are configurable as a separate LUT file within the Ancillary Data Sets. For examples use to demonstrate operation in this ATBD, physical and optical properties (Table 7) are derived from a set of 40 predefined aerosol mixtures (Holzer-Popp et al., 2008), used in the ESA Synergy Project. These external mixtures are based on 6 principal aerosol components as given in Table 6. Refractive Index and log-normal size distributions of each of the components are derived from the Optical Properties of Aerosols and Clouds (OPAC) aerosol models (Hess, 1998) specified by the Global Aerosol Data Set (GADS).

The Angstrom coefficient, single scattering albedo and phase function are derived for each mixture in advance, from microphysical characteristics using Mie theory, and are necessary to parameterise the RT model to generate the LUT coefficients. In order to report retrieved aerosol properties, a further table stores the properties indexed by aerosol model number. These properties are Angstrom coefficient α , at a reference wavelength (550 nm), Single Scattering Albedo (SSA) at each waveband and phase function $P(\Theta)$ at each waveband, where Θ denotes the scattering phase angle).

4.5.4 LUT approximation of RT coefficients

Prior to operation a look-up table (LUT) is constructed to allow rapid run-time estimation of the quantities R_{atm} , T , ρ_{atm} by interpolation. In addition for the inversion we require a pre-computed

estimate of $D(\theta_s)$ at each waveband, defined as the fraction of total downwelling light at the surface which is diffuse, defined at a fixed surface albedo (0.2). These quantities are pre-computed using an accurate radiative transfer model; in testing the model the MOMO atmospheric radiative transfer code model (Fell and Fischer, 2001, Rathke and Fischer, 2002) was used; however use of other accurate radiative transfer codes is possible. It is most efficient in space to have a separate LUT for each of the 4 terms, as they have different dimensions.

The lookup table dimensions are:

- $R_{atm}(\lambda, H_2O, p_s, \tau_{550}, \theta_v, \theta_s, \phi)$ [7 dimensions]
- $T(\lambda, H_2O, p_s, \tau_{550}, \theta_v, \theta_s)$ [6 dimensions]
- $\rho_{atm}(\lambda, H_2O, p_s, \tau_{550})$ [4 dimensions]
- $D(\lambda, p_s, \tau_{550}, \theta_s)$ [4 dimensions]
- $C_{O_3}(\lambda)$ [1 dimension]

where p_s denotes surface pressure (hPa), λ denotes waveband, and H_2O water vapour ($g\ cm^{-2}$). For calculation of diffuse fraction D , a fixed water vapour level ($2\ g\ cm^{-2}$) can be used. A set of LUTs is required for each aerosol model.

The points required for angular sampling of each dimension are as stated in Table 6, plus AOD, surface pressure and water vapour (WV) stated in Table 7, and aerosol model index (Table 8). The coefficients are required for all wavebands, with the exception of the absorption channels (Table 5).

From the density of the lookup table grid points and the comparatively smooth behaviour of the TOA reflectance as a function of the LUT dimensions, we can estimate that the error introduced by the LUT approach and the employed linear interpolations is considerably smaller than the expected uncertainties due to selection of aerosol model parameters. Figure 2 illustrates the relation of surface to TOA reflectance for differing levels of AOD.

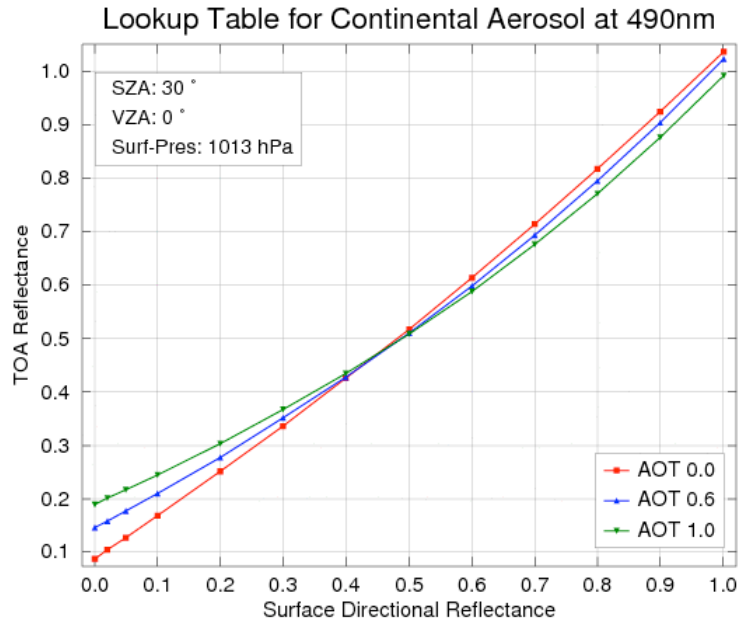


Figure 2: Relation of TOA to surface reflectance by lookup table

4.5.5 Estimation of surface reflectance

During operation we use multidimensional piecewise linear interpolation to obtain the required atmospheric coefficients (R_{atm} , T , ρ_{atm} , $D(\theta_s)$) for given solar/view geometry, waveband, AOD, aerosol type, column water vapour and surface pressure. The value T_{O_3} is determined from (5). A linear model is applied between neighbouring grid points in all dimensions.

By rearranging (2), the quantity R_{surf} can readily be derived from R_{TOA} by

$$R_{surf}(\theta_v, \theta_s, \phi) = \frac{f}{1 + \rho_{atm} f} \quad (6)$$

where

$$f = \frac{R_{TOA}(\theta_v, \theta_s, \phi) / T_{O_3} - R_{atm}(\theta_v, \theta_s, \phi)}{T(\theta_v, \theta_s)} \quad (7)$$

This procedure provides an atmospherically corrected surface directional reflectance (SDR), also referred to as Lambert equivalent reflectance (LER) or bidirectional reflectance factor (BRF). Note that different values of SDR will be retrieved for different view directions.

Table 6: Sun-sensor geometry used in the LUT for SLSTR, OLCI.

Parameter	Range	Interval	Number of breakpoints
RAZ	0 - 180°	6°	30
SZA	0 - 70°	Variable depending on Gaussian integration 3.5° (mean interval)	20
VZA		Variable depending on Gaussian integration	
- SLSTR nadir	6 - 58°	3° (mean interval)	18
- SLSTR along-track	55°	Constant at 55°	1
- OLCI	0 - 55°	3° (mean interval)	18

Table 7: Parameters used in LUT for all instruments

Aerosol properties	
-AOD at 550 nm	0.0, 0.05, 0.1, 0.2, 0.4, 0.6, 1.0, 1.5, 2.0, 3, 4 The Angstrom coefficient, single scattering albedo and phase function will be derived from 40 aerosol models of different mixtures of 6 components aerosol types from refractive index, and Junge size distribution.
Surface pressure	1030, 1000, 900, 800 hPa corresponding to elevation variation of 0 – 2500 metres.
Water vapour	0, 2, 5 g cm ⁻²

Table 8: Aerosol types calculated from external mixtures from 6 basic components

No.	Name	Humidity	Height	Water soluble	Water insoluble	Sea salt accumulation mode	Sea salt coarse mode	soot	Mineral transported
1	Pure Watersoluble	50%	2 km	100					
2	Continental I	50%	2 km	95	5				
3	Continental II	50%	2 km	90	10				
4	Continental III	50%	2 km	85	15				
5	Maritime I	50%	2 km	30		70			
6	Maritime II	50%	2 km	30		65	5		
7	Maritime III	50%	2 km	15		85			
8	Maritime IV	50%	2 km	15		75	10		
9	Polluted Watersoluble I	50%	2 km	90				10	
10	Polluted Watersoluble II	50%	2 km	80				20	
11	Polluted Continental I	50%	2 km	80	10			10	
12	Polluted Continental II	50%	2 km	70	10			20	
13	Polluted Maritime I	50%	2 km	40		45	5	10	
14	Polluted maritime II	50%	2 km	30		40	10	20	
15	Desert Outbreak I	50%	4 km	75					25
16	Desert Outbreak II	50%	4 km	50					50
17	Desert Outbreak III	50%	4 km	25					75
18	Biomass Burning I	50%	3 km	85				15	
19	Biomass Burning II	50%	3 km	70				30	
20	Biomass Burning III	50%	3 km	55				45	
21-40	Humid version (=1-20)	80%							

4.6 Constraints on surface reflectance

To retrieve estimates of aerosol properties from measured satellite radiances, we need to solve the inverse problem to separate the atmospheric and surface scattering contributions to the observed signal. This normally requires some assumptions to be made on the land surface brightness. Within the proposed framework, these assumptions are expressed as constraints defined by error of fit to a parameterized model describing the surface angular or spectral reflectance.

For synergistic retrieval, we combine the main methods used for global aerosol retrieval from optical imagery; these are the dark object method (DOM) and multiple view-angle (MVA) methods, building on existing work for MERIS and AATSR, respectively. In principle other constants can be employed within the inversion framework, and the method updated to include best available constraints. Note that either spectral or angular constraint can be applied in isolation; in areas of swath not including the off-nadir-view SLSTR look the spectral constraint can be applied alone, though with some loss of accuracy.

4.6.1 Dark object constraint

When viewing from a single direction, we must rely on the spectral signature to distinguish aerosol from ground scattering. For a given set of surface reflectances derived by assuming a certain atmospheric profile, this may be expressed as an error based on the fit of the retrieved surface reflectance to the assumed target reflectance. This allows estimation retrieval of the atmospheric aerosol by optimal estimation. Where a target of approximately known reflectance can be identified,

such as dense vegetation or a body of water, aerosol optical depth at the target location may be estimated on the basis of known correlation of ground reflectance at different wavelengths ([Remer et al., 2005]). The first stage in such schemes is the identification of dark pixels. One approach to identifying dark pixels is to calculate the Normalized Difference Vegetation Index (NDVI):

$$NDVI = \frac{\rho_{870} - \rho_{670}}{\rho_{870} + \rho_{670}} \quad (8)$$

where ρ_{870} and ρ_{670} are the TOA reflectances in the near infrared and red region, respectively. These approaches can be applied to any values of NDVI greater than a set threshold.

Where a large number of wavebands are available as in the case of OLCI/SLSTR it is possible to represent the target reflectance as a linear mixture of an idealized vegetation and soil spectrum, or set of spectra using:

$$\rho_{spec_mod}(\lambda) = C_{veg}\rho_{veg}(\lambda) + C_{soil}\rho_{soil}(\lambda) \quad (9)$$

where C_{veg} and C_{soil} are the fractional coverage of vegetation and soil respectively. They may sum to greater than one (equivalent to scaling brightness of these components) and the two fractions are the free parameters that we retrieve. The ρ_{surf} , ρ_{veg} and ρ_{soil} term are the surface reflectance, vegetation and soil reflectance of the input spectra, respectively and are a function of wavelength. A number of variations on such methods have been used successfully for aerosol retrieval with MERIS (von Hoyningen-Huene et al., 2006; Guanter et al., 2007; Santer et al., 2007). However, routine application is limited to regions where such targets are available at the appropriate spatial resolution (i.e. oceans and dark dense vegetation), and accuracy is limited to the level of uncertainty in the *a priori* estimate of target reflectance variation. In operation the spectra ρ_{veg} and ρ_{soil} will be configurable in the input data file.

4.6.2 Multiple View-Angle (MVA) constraint

We have developed a method for simultaneous estimation of AOD and surface reflectance for data where at least two view angles are available, such as the AATSR (North et al., 1999; North 2002; Grey et al., 2006a,b). Methods employing similar principals have also been developed for AATSR and other multi-view sensors, (Veefkind et al., 1999; Diner et al., 2005; Kokhanovsky et al., 2007). The principal advantage of this approach is that no *a priori* information of the surface is required and aerosol properties can be retrieved even over bright surfaces. In the case of multi-view-angle data, a constraint may be made on the angular variation of the land surface reflectance, governed by the BRDF, giving a corresponding error of fit. In particular, the angular variation is assumed to be approximately constant across wavelength, since the angular variation (i.e. shape of the surface bi-directional reflectance distribution) is due principally to geometric effects (e.g. shadowing) which are wavelength independent. This means that for SLSTR, the ratio of surface reflectances at the nadir and off-nadir viewing angles (where the view zenith angle is 55°) is well correlated between bands. This avoids the need for assumptions on absolute surface brightness or spectral properties. The method presented here differs from early approaches by using a more sophisticated surface model

to account for some spectral variation of the angular shape owing to the variation of the diffuse fraction of light with wavelength.

Scattering of light by atmospheric aerosols tends to be greater at shorter wavelengths. It is important to model the fraction of diffuse to direct radiation since it influences the anisotropy of the surface. The anisotropy is reduced when the diffuse irradiance is high because the contrast between shadowed and sunlit surfaces decreases. Anisotropy is similarly dependent for bright targets owing to the multiple-scattering of light between the surface elements. The atmospheric scattering elements including aerosols and gas molecules are comparable in size to the wavelength of light at optical wavelengths. As a result, the effect of atmospheric scattering on the anisotropy will be a function of wavelength and the shape of the BRDF will vary. Taking these effects into account results in a physical model of spectral change with view angle ([North et al., 1999]) :

$$\rho_{ang_mod}(\lambda, \Omega) = (1 - D(\lambda))v(\Omega)w(\lambda) + \frac{\gamma w(\lambda)}{1 - g} [D(\lambda) + g(1 - D(\lambda))] \quad (10)$$

where $g = 1 - \gamma w(\lambda)$, λ is the wavelength, Ω is the viewing geometry (forward or nadir view in the cases of AATSR), ρ_{mod} is the modelled bidirectional reflectance, γ is the fraction contributing to higher-order scattering and is fixed at 0.3, and D is the fraction of diffuse irradiance. The model separates the angular effects of the surface into two components, a structural parameter v that is dependent only on the viewing and illumination geometry, and the spectral parameter w , that is dependent only on the wavelength. The free parameters that we need to retrieve through model inversion are $w(\lambda)$ and $v(\lambda)$.

By inversion of (10), this model of surface scattering has been shown theoretically to lead to a tractable method which is potentially more robust than the simple assumption of angular invariance alone (North 1999). The angular reflectance of a wide variety of natural land surfaces fits this simple model. In contrast, reflectance that is a mixture of atmospheric and surface scattering does not fit this model well. As a result, the model can be used to estimate the degree of atmospheric contamination for a particular set of reflectance measurements and to find the atmospheric parameters which allow retrieval of a realistic surface reflectance.

Next we combine these two surface constraints within the scheme of a numerical inversion framework to simultaneously obtain an optimal estimate of surface reflectance and aerosol.

4.7 Numerical inversion

The retrieval algorithm is illustrated in Figure 1. To retrieve the aerosol properties from TOA cloud-free radiances we use a coupled numerical inversion scheme that incorporates the lookup tables derived from the radiative transfer model and a constraint based on a simplified model of land surface scattering. The basis of the inversion is (i) estimation of surface reflectance (R_{SURF}) for all bands and view angles, for an initial estimate of atmospheric profile, and (ii) iterative refinement of the atmospheric profile to minimise an error metric (E_{MOD}) on the retrieved surface reflectance set.

4.7.1 AOD retrieval

The input to the algorithm is the merged TOA product, averaged over a 8km x 8km window for each retrieval. This resolution is appropriate to minimise the effect of errors in image registration, while retrieving aerosol within the spatial scale of aerosol variability (North, 2002). A set of surface reflectances are calculated for a given atmospheric aerosol model and AOD parameterised by value at 550 nm. An error metric is defined on the surface reflectance set based on a weighted combination of the DOM and MVA constraints:

$$E_{\text{mod}} = \frac{1}{12} \sum_{\Omega=1}^2 \sum_{\lambda=1}^6 w_{\lambda,\Omega} [\rho_{\text{surf}}(\lambda, \Omega) - \rho_{\text{ang_mod}}(\lambda, \Omega)]^2 + \frac{1}{N} \sum_{\lambda=1}^N w_{\lambda} [\rho_{\text{surf}}(\lambda) - \rho_{\text{spec_mod}}(\lambda)]^2 \quad (11)$$

where $\rho_{\text{spec_mod}}$ and $\rho_{\text{ang_mod}}$ are the surface reflectances estimated using (9) and (10) respectively, based on the best-fit values of the free parameters, and ρ_{surf} is the surface reflectance calculated using (6). Iterative inversion yields the optimal values of the free parameters (AOD and aerosol model).

To optimize the performance of the inversion, normalised values for the set of weights w_i are determined for each constraint (angular and spectral) separately. For the angular model, the six SLSTR channels are weighted as follows: {1.5, 1.0, 0.5, 1.0, 1.0} for both nadir and forward views. For the spectral model, all channels have weights of 1.0 for channels in the range 400-700nm, and for 1610-2250, and 0.05 for remaining channels. Each set of weights are normalised to 1. These weights will be configurable post-launch to optimise performance.

The relative weighting between the angular and spectral models is based on the NDVI and thresholds. The spectral weight is always (1 - angular weight) for normalisation. The angular weight is 1 for NDVI less than 0.1. For the interval [0.1, 0.7] the angular weight changes linearly from 1.0 (for NDVI = 0.1) to 0.5 (for NDVI = 0.7). In the NDVI range [0.7, 1.0] the angular and spectral weight is 0.5.

For a given atmospheric profile the optimal free parameters of the separate land surface models that minimize (9) and (10) are found through the *Powell* multi-dimensional minimisation routine (Press et al., 1992). This process is repeated for different AOTs and aerosol models. The optimal aerosol properties are found using the Brent one-dimensional optimisation method, by finding the value of atmospheric AOT which give rise to the lowest value of E_{MOD} in (11).

4.7.2 Selection of optimal aerosol model

The optimal aerosol model is selected by search for the aerosol model which minimises the estimated error from (11) Retrievals are run independently with different candidate models, and minimum value of E_{MOD} across the range of models provides an estimate for most likely aerosol type and corresponding properties of Angstrom coefficient, single scattering albedo and phase function. The operation should be configurable to optionally include exhaustive search for minima over all models, or specify a single aerosol model, or regional subset of models.

Figure 3 illustrates inversion procedure and the potential to distinguish between the set of aerosol models. The inversion is run on TOA data for the Tomsk test site. The figures show retrieval where each aerosol model is applied in turn; the figure 'Aerosol Model Comparison' shows the range of AOD and corresponding f_{min} . The figures show the value of the error metric defined for spectral and angular constraints, and for the combined (Synergy) constraint. In this case the lowest value is given by biomass burning model, which would be returned by the algorithm; however in this case all models except urban give similar errors of fit. A further example of retrieval over an image is shown in Figure 10 for Beijing.

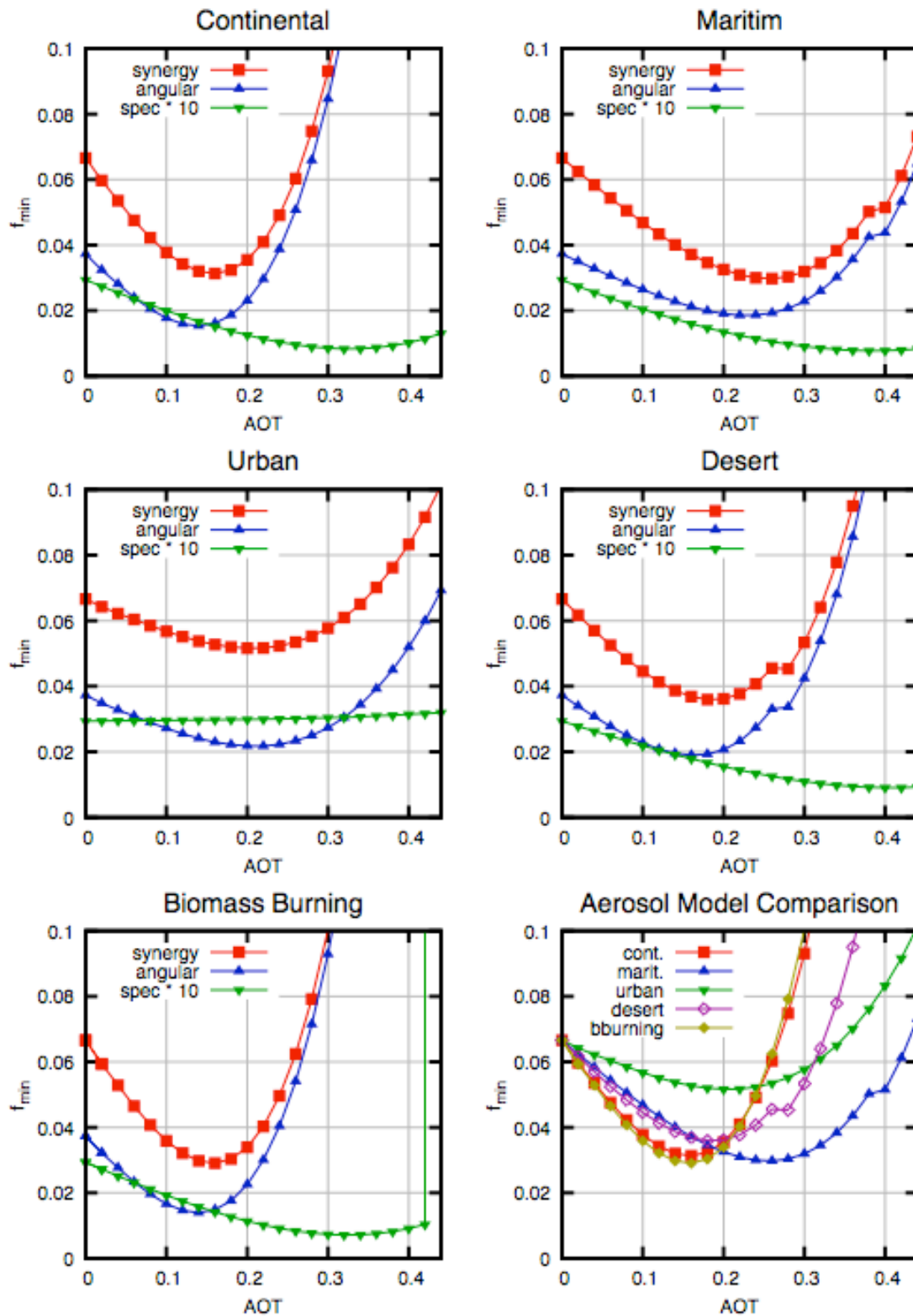


Figure 3. Plots for Tomsk showing retrieval for a range of possible aerosol models.

4.8 Retrieval error estimate

4.8.1 Error in AOD

The error in retrieving optical thickness is estimated from the error metric E_{mod} of the fit from (11), and the curvature of the error surface near the minimum. The optimization procedure determines the minimum E_{min} of $E_{mod}(\tau)$, where τ represents the aerosol optical thickness defined at a reference wavelength (550nm). The value τ_{min} , where $E_{mod}(\tau_{min}) = E_{min}$, is the resulting aerosol optical thickness. The curvature term (a) of a parabolic fit to the error metric $E_{mod}(\tau)$ is calculated near the minimum. This curvature term allows calculation of the uncertainty of the retrieved aerosol optical thickness τ_{min} . This uncertainty (1 s.d.) can be expressed as:

$$\Delta\tau = k\sqrt{\frac{E_{min}}{a}} \quad (12)$$

The curvature term (a) of the error surface gives a measure of the sensitivity of the location of the minimum to error in model fit. For a steeply curved error surface, the retrieved value of t is relatively robust to the estimation of model fit, while for a flat error surface small perturbation in model fit error gives rise to a large error in τ . As surface reflectance approaches the ‘critical point’, where the TOA radiance is insensitive to variation in τ , then a approaches 0 and we have high uncertainty in τ . Similarly high values of a are found where deviation of TOA reflectance is greatest with small change in τ , which is expected for high contrast between aerosol and surface scattering, i.e. for low AOT and dark surfaces. The term E_{min} gives a sample of the combined error due to error in radiative transfer model, instrument noise, and deviation of surface reflectance from the assumed reflectance model. The term k is estimated to be 1.58, but this value should be improved by post-launch calibration of retrieved AOD against sun-photometer data.

4.8.2 Surface reflectance error

The error in surface reflectance at each waveband is calculated as the sum of errors due to the error in AOD estimation Δ_{τ} , sensor noise Δ_{sens} , and estimated error in the radiative transfer model Δ_{RT} . For each channel, the uncertainty is given by

$$\Delta R_{surf} = \left(\Delta_{\tau}^2 + \Delta_{sens}^2 + \Delta_{RT}^2 \right)^{0.5} \quad (13)$$

The uncertainty in surface reflectance due to aerosol error is

$$\Delta_{\tau} = \frac{\delta R_{surf}}{\delta \tau} \Delta \tau \quad (14)$$

Where $\Delta \tau$ is obtained from (12). An estimate for $\delta R/\delta \tau$ at each wavelength is given by linear fit of the variation of R with τ near τ_{min} , using surface reflectance at the same two points as used to find the parabola parameter a . We estimate error in surface reflectance Δ'_{sens} due to instrument noise in the TOA measurement Δ'_{sens} using:

$$\Delta_{sens} = \frac{\delta R_{surf}}{\delta R_{TOA}} \Delta'_{sens} \approx \frac{\Delta'_{sens}}{T_{O_3} T(\theta_s) T(\theta_v)} \quad (15)$$

Estimate of the channel-dependent instrument noise Δ'_{sens} should include the combined effects of quantisation and calibration error. The error in the radiative transfer model Δ_{RT} includes the net effect of numerical approximation of atmospheric radiative transfer variation and composition (column ozone, water vapour and aerosol model) from reality. A value of 0.005 should be used as default.

4.9 Atmospheric correction over land

Accurate atmospheric correction is essential for quantitative estimation of surface biophysical properties such as fAPAR and albedo, and for separation of changes in surface state over time from changes in the atmosphere. Here we use the improved characterisation of atmospheric aerosol to derive improved surface reflectance from the OLCI and SLSTR instruments. The input for this algorithm is the TOA reflectance for all channels, and the derived fields of aerosol model and AOD, column water vapour and ozone and surface pressure.

4.9.1 Aerosol Parameter Interpolation (API)

An optimal estimate of surface reflectance for each channel is produced from the aerosol retrieval procedure. However, this is obtained at a coarser grid than the original image (8 x 8 pixels), and may contain missing values where the inversion has not converged. For atmospheric correction we need a further step to interpolate AOT values to all pixels within the image. This is achieved by an iterative coarse-to-fine filtering procedure, which preserves original retrieved AOT values and estimates AOT where there is missing data. Uncertainty in AOD is also interpolated. Bilinear interpolation is sufficient for estimating these values.

The interpolation algorithm is defined as follows:

For a given pixel with image coordinates (m,n), with no AOD value found by retrieval, fill with a value f_{interp} by bilinear interpolation of values from four surrounding points. These points are found by iteratively increasing a box of side d pixels surrounding the point, until at least four points are enclosed; if more than 4 then the nearest enclosing 4 are selected.

For retrieved values f_x defined at point coordinates $f_1(j_0, k_0)$, $f_2(j_1, k_0)$, $f_3(j_0, k_1)$ and $f_4(j_1, k_1)$, the interpolated value f_{interp} is given by

$$f_{\text{int}} = \left((j_1 - j_0)(k_1 - k_0) \right)^{-1} \begin{pmatrix} f(j_0, k_0)(j_1 - m)(k_1 - n) + \\ f(j_1, k_0)(m - j_0)(k_1 - n) + \\ f(j_0, k_1)(j_1 - m)(n - k_0) + \\ f(j_1, k_1)(m - j_0)(n - k_0) \end{pmatrix} \quad (16)$$

A final median filter is applied on a 3 x 3 moving window to improve robustness by eliminate outlying retrievals. The same lookup tables of atmospheric parameters developed for the aerosol retrieval algorithm are used to produce surface reflectances across the image for the overlapping image region of OLCI and SLSTR, using (6), and their uncertainties using (13).

Figure 4 demonstrates this processing on a scene from MERIS/AATSR for 15/05/2003 over the Tomsk Aeronet station. The TOA false colour RGB (R = nadir1610, G = nadir865, B = fward550) is shown in the top left panel, the atmospherically corrected RGB (same channels) is shown in the top right. The retrieved AOT is shown in the middle row left panel. The gaps due to cloud screening or failed retrievals are clearly visible. The lower two right panels show the two filled AOT products: Centre right panel shows the results after an iterative box car extrapolation. The image in the lower right shows the result after application of an additional median filter to the gap filled image.

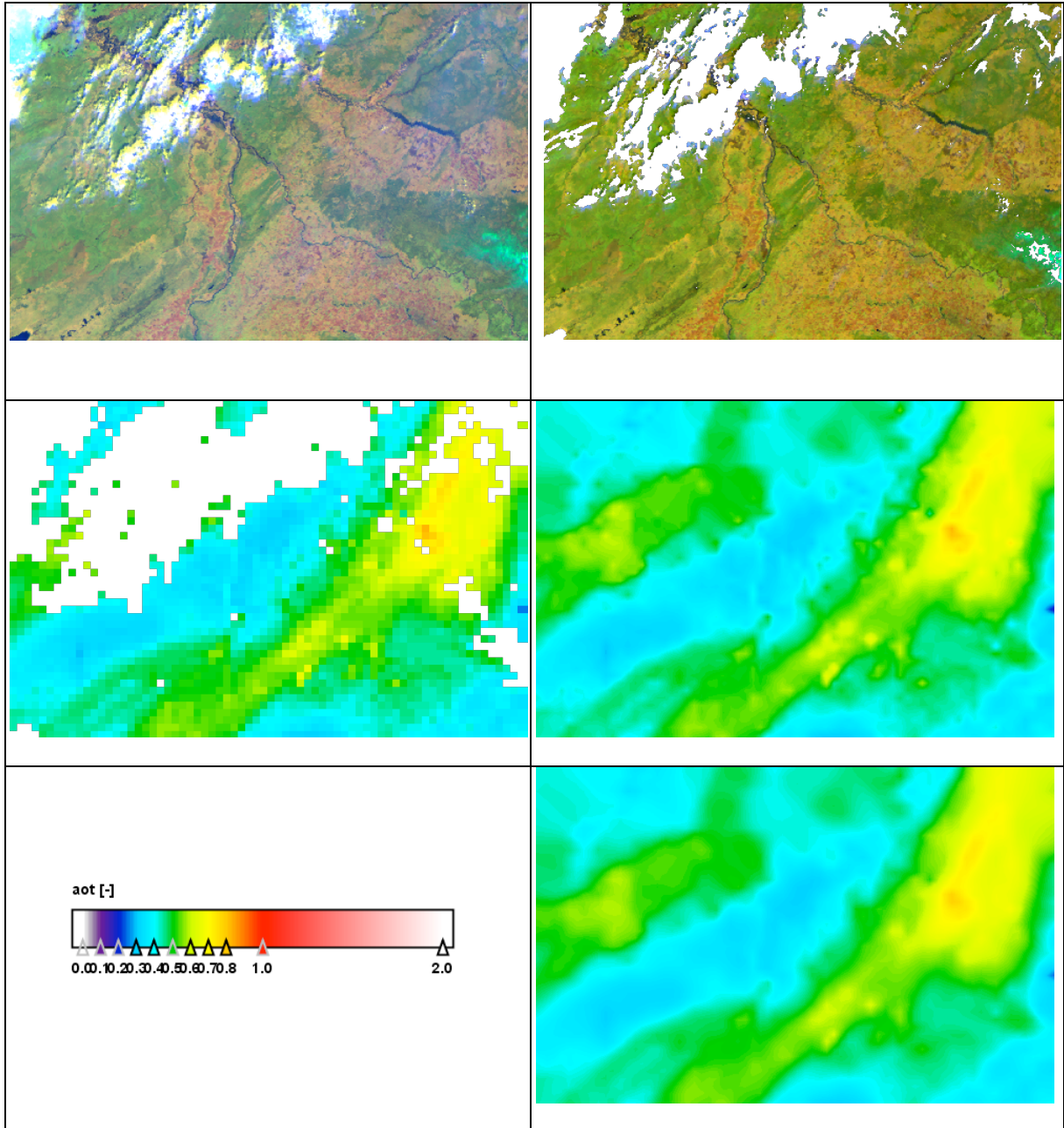


Figure 4. Tomsk site (15/5/2003) showing interpolation of aerosol field and atmospheric correction. False colour TOA image is shown (top left), and retrieved image of surface directional reflectance (top right). Retrieved AOT is shown with gaps (centre left), after interpolation (centre right) and) after median filter smoothing (lower right).

4.10 Summary of products

The following products are returned by the procedure:

- Atmospherically corrected surface directional reflectance (SDR) at all OLCI and SLSTR wavebands, other than within gaseous absorption bands (O_2 , H_2O), and uncertainties:
 - SYN_SDR_1_OLCI... SYN_SDR_21_OLCI
 - SYN_SDR_nadir_1_SLSTR... SYN_SDR_6_SLSTR
 - SYN_SDR_off_nadir_1_SLSTR... SYN_SDR_off-nadir_6_SLSTR
 - SYN_SDR_uncertainty_1_OLCI... SYN_SDR_uncertainty_21_OLCI
 - SYN_SDR_uncertainty_nadir_1_SLSTR...
SYN_SDR_uncertainty_nadir_6_SLSTR
 - SYN_SDR_uncertainty_off_nadir_1_SLSTR... SYN_SDR_uncertainty_off-nadir_6_SLSTR
- *aot*: AOT (with gaps) at reference waveband (550nm)
- *aot_filled*: retrieved AOT gap filled
- *aot_filter*: AOT gap filled then 3x3 median filtered
- *aot_uncertainty*: retrieved uncertainty of AOT
- *aot_uncertainty_filled*: uncertainty with gaps extrapolated
- *land_aerosol_model*: Aerosol model index number
- *land_aerosol_model_filled*: model number constant extrapolated to gaps
- *aerosol_land_flags*: flags containing information on the retrieval:
 - pixel detected partly cloudy
 - pixel partly not land
 - AOT successfully retrieved
 - Border pixel, means the average for the retrieval is based on fewer pixels because the pixel is at the border of the scene.
 - AOT filled
 - AOT retrieval failed with negative error metric curvature
 - AOT retrieval failed because AOT too low ($AOT < 1e-5$)

- AOT retrieval failed because relative error is too high ($AOT > 0.1$ and relative uncertainty $> 500\%$)

For failed retrievals, last three flags, are flagged but reported in the AOT product. However for the gap filled products, only successful retrievals are used.

4.11 Accuracy assessment

A prototype of the algorithm has been implemented within the BEAM processor, and tested on sets of simulated and real satellite data using AATSR and MERIS. Full description of algorithm performance on real data is given in the associated Synergy ATBD and Synergy Product Validation Report (PVR); examples are shown here to demonstrate operation and evaluate expected performance.

4.11.1 Test sites and instrument co-location

A dataset of 68 image sets has been established for testing and validation of synergy algorithms, targeting sites with existing AERONET sun photometer measurements (Table 9). The sites cover a range of surface types and sources of aerosol, and include examples of cloudy and clear scenes. The data are smile-corrected for MERIS using the existing BEAM processor. The smile effect refers to the fact that across the field-of-view the characteristics of the optics and slight misalignments of the sub-systems generally induce small variations of the spectral channels central wavelength.

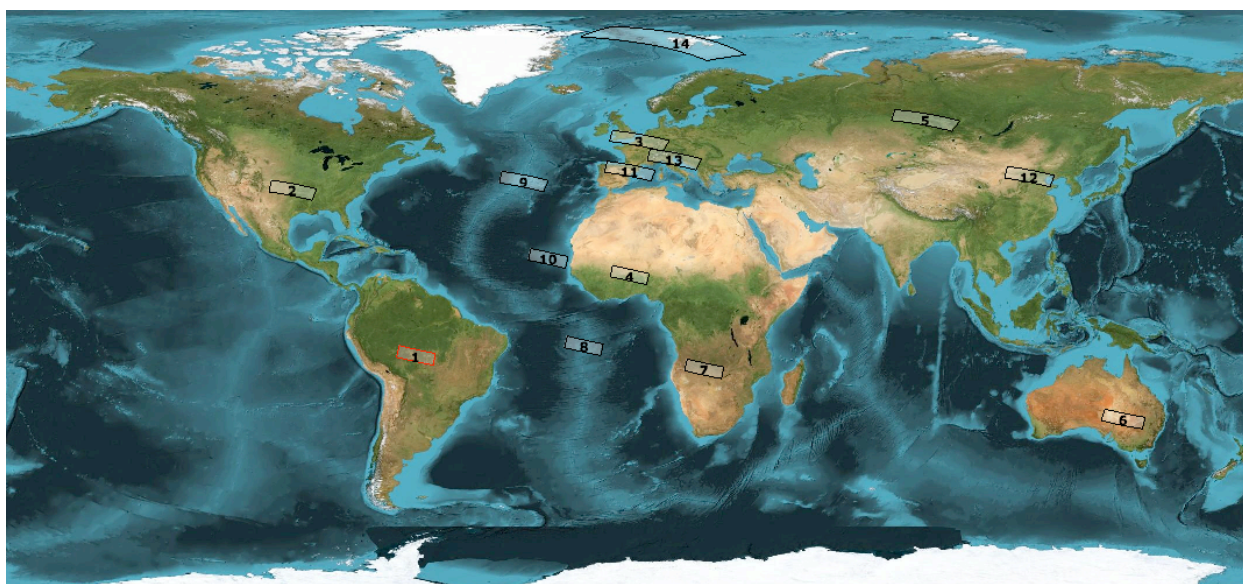


Figure 5. Location of image sets selected for aerosol retrieval validation.

Table 9. Test site location and cover type

Site name	Lat.	Long	Cover type	<i>n</i>
Abracos_Hill	-10.8°N	-62.4°E	Forest	8
Beijing	40.0°N	116.4°E	Urban	6
Cart_Site	36.6°N	-97.5°E	Grassland	7
Lille	50.6°N	3.1°E	Urban	4
Mongu	-15.3°N	23.2°E	Semi-arid	8
Ouagadougou	12.2°N	1.4°E	Semi-arid	23
Tinga Tingana	-29.0°N	140.0°E	Semi-arid	6
Tomsk	56.5°N	85.1°E	Forest	4
Barcelona	41.39°N	2.12°E	Coastal	2

4.11.2 Evaluation on satellite imagery

The Synergy project Product Validation Report documents operation of the algorithm on all scenes, and gives a full comparison of the algorithm retrieval with Aeronet and with the MERIS L2 DDV algorithm (Santer et al. 2005), and the MERIS spectral algorithm IBAER (von Hoyningen-Huene et al., 2006). Here we discuss several examples of the algorithm output, and summarise the main results of the comparison with AERONET.

- **Lille (14/7/2003)** Figure 6 shows performance of the Synergy retrieval over the Lille test site (50.6°N, 3.1°E), for 14/7/2003. Here consistent AOT is retrieved throughout the scene in the range 0-0.2. The AERONET value at Lille is 0.09, compared with the Synergy retrieval of 0.145. Here both spectral and angular constraints have similar weighting, where spectral alone would give an estimate of 0.25, and angular alone 0.05.
- **Ouagadougou (6/2/2003)** Figure 7 shows retrieval over the Ouagadougou test site (12.2°N, 1.4°E), on 6/2/2003. The value at the AERONET station is 0.297, compared with the Synergy retrieval of 0.23. Over this relatively bright scene the retrieval is dominated by the angular constraint.
- **Abracos Hill (31/7/2005)** Figure 8 shows the Synergy retrieval over the Abracos Hill test site (-10.8°N, -64.4°E), for 31/7/2005. The surface cover is tropical forest, with significant areas of clearance, especially near the AERONET site. The retrieved value of AOT by the Synergy algorithm over the AERONET station is 0.76 at 550nm, which compares with a measured

AERONET value of 0.83. Here the retrieval is dominated by the spectral constraint, which alone would have resulted in AOT of 0.78; in this instance the angular constraint alone would have lead to very high error (retrieval of 0.25). This region is known to be difficult for the angular retrieval alone, with typical underestimation of AOT (Bevan et al., 2009).

- **Beijing (20/4/2006)** Figure 9 shows performance of the Synergy retrieval over the Beijing test site (40.0°N, 116.4°E), on 20/4/2006. The results show high disagreement between the three retrieval schemes. Here the Synergy algorithm retrieves a value of 0.24 over the AERONET site, while the ground measurement is also 0.24. Here the bright surface results in a relatively high weighting for the angular constraint.

Lille (20030714)

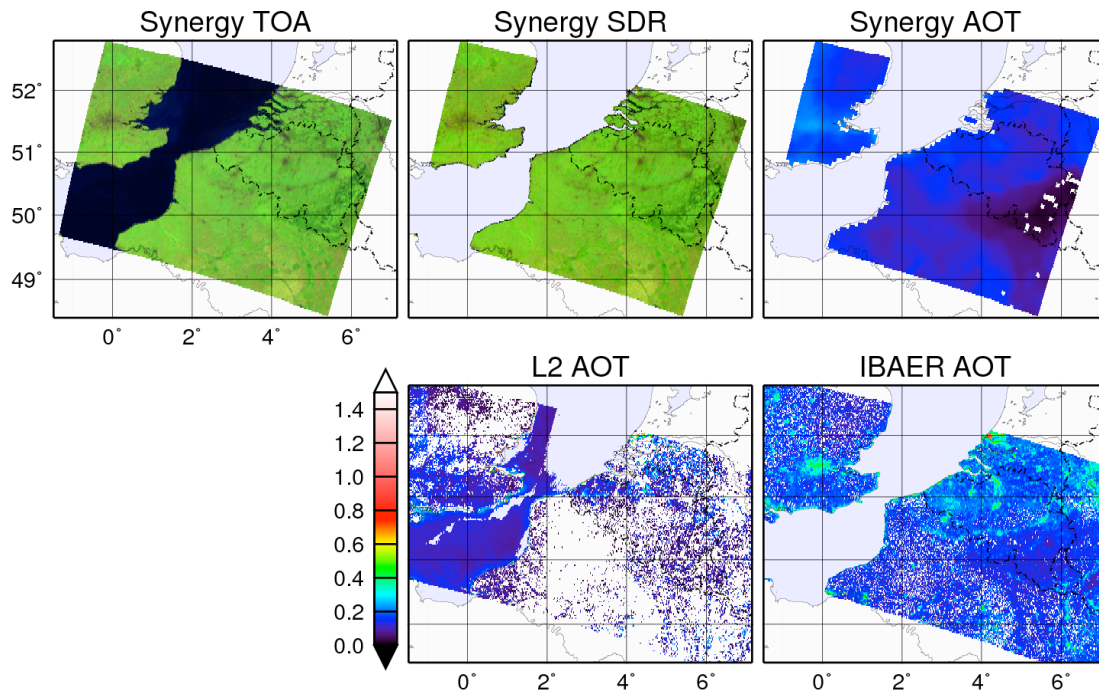


Figure 6. Results of Synergy Retrieval over Lille site, 14/7/2003.

Ouagadougou (20030206)

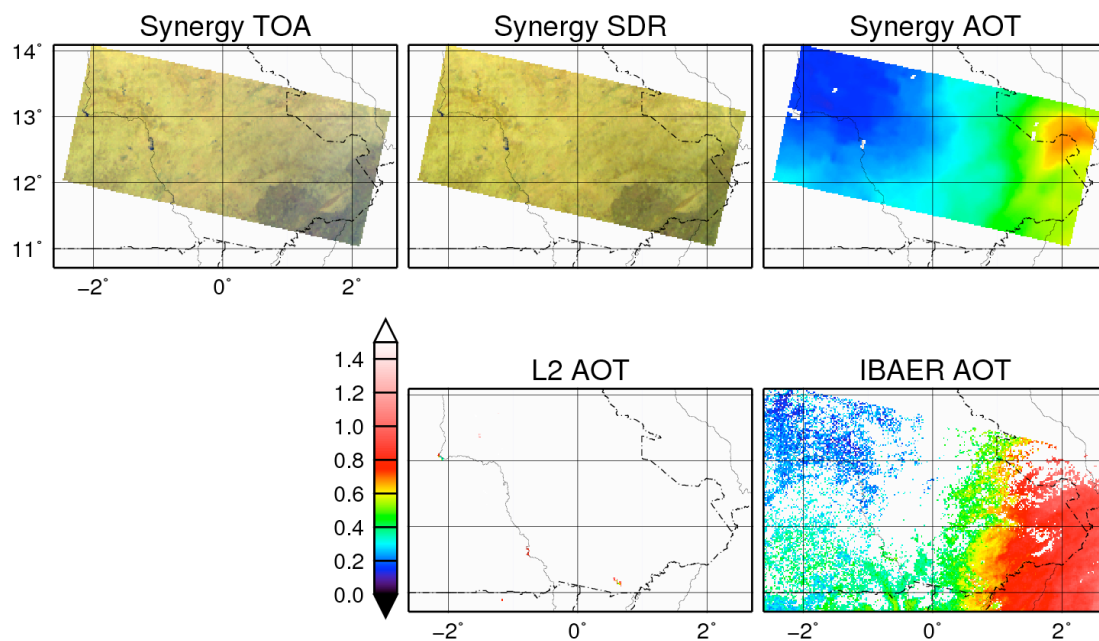


Figure 7. Results of Synergy Retrieval over Ouagadougou site, 6/2/2003.

Abracos_Hill (20050731)

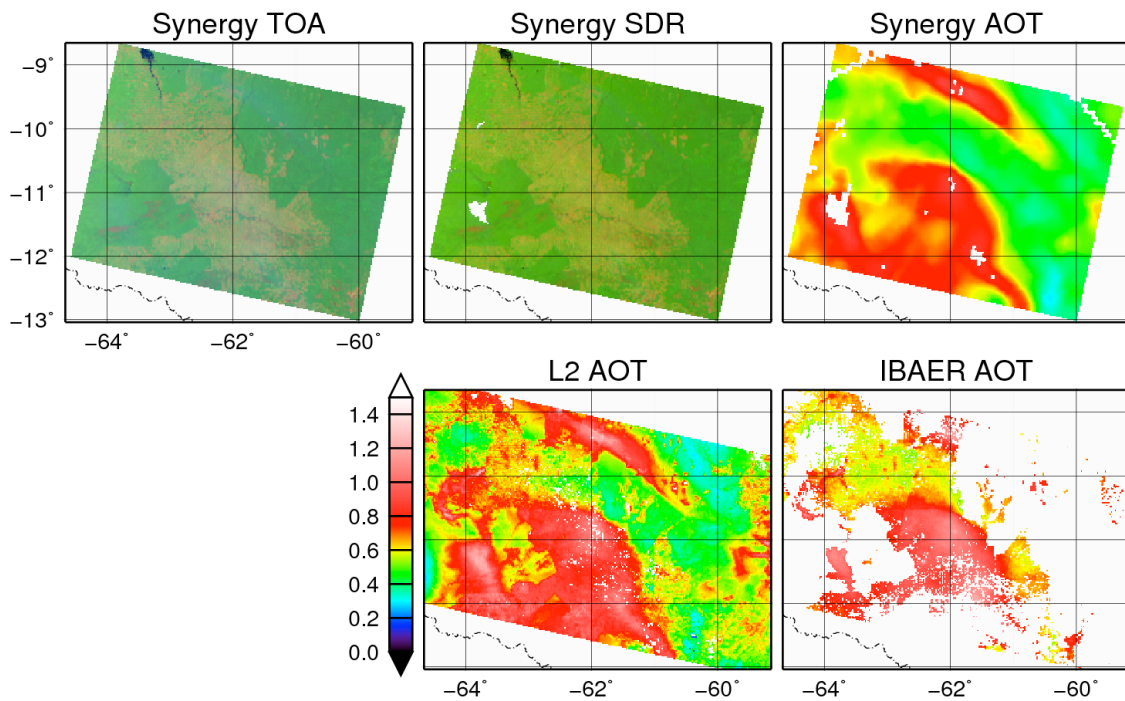


Figure 8. Results of Synergy Retrieval over Abracos Hill site, 31/7/2005.

Beijing (20060420)

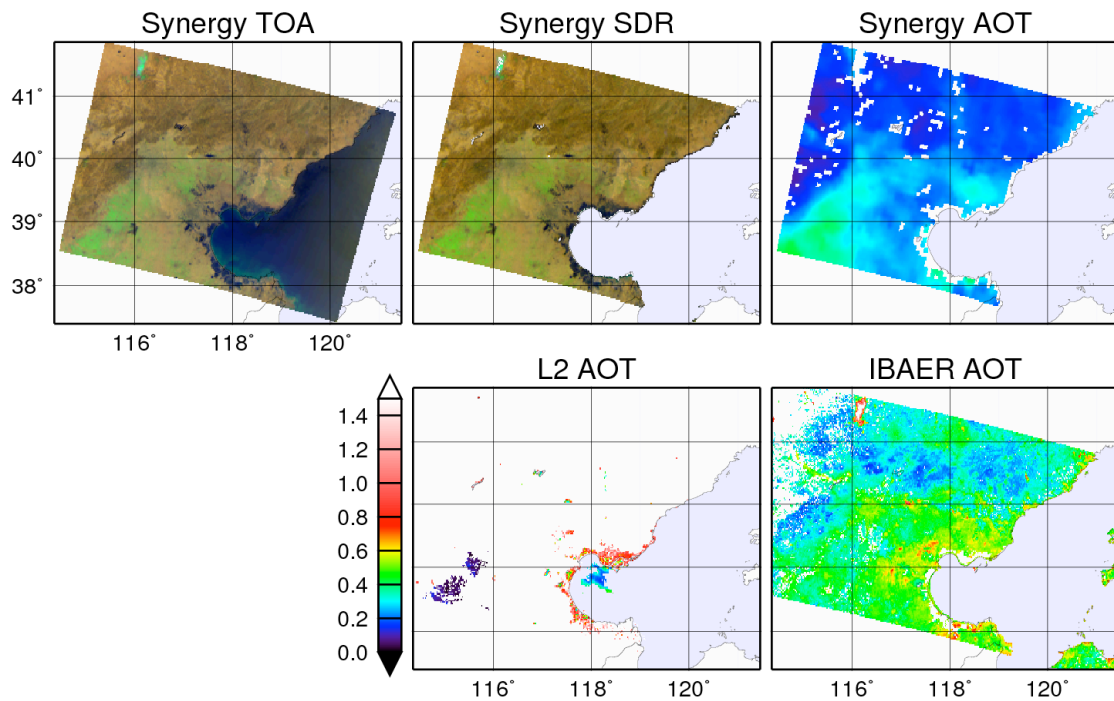


Figure 9. Results of Synergy Retrieval over Beijing site, 20/4/2006.

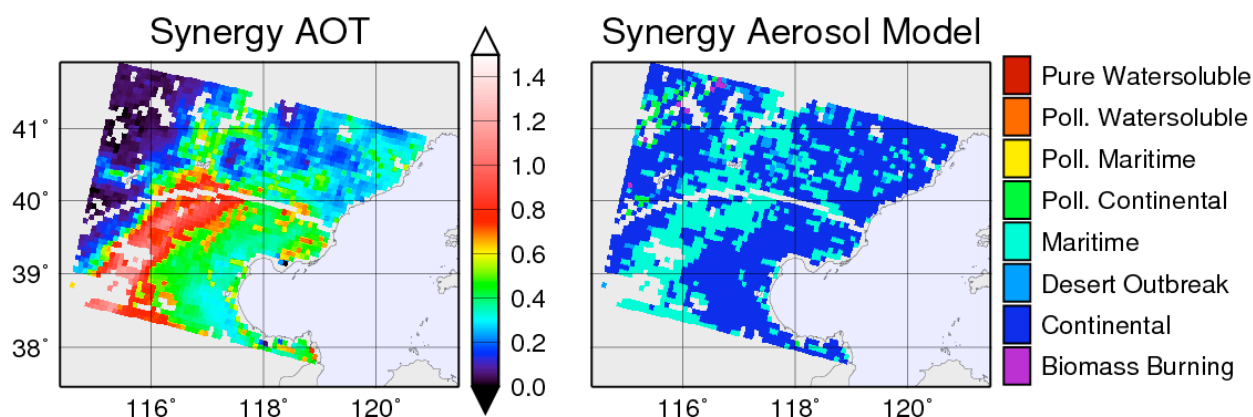


Figure 10. Plots for Beijing (12/10/2006) showing retrieval for a range of possible aerosol models. Retrieval is mainly discriminated by size distribution; here the retrieval indicates larger particle size (classified as maritime model) within the high concentration aerosol region, with predominantly the fine particle model (continental) retrieved throughout the remainder of the image. The arc of missing values corresponds to dropout pixels within the AATSR scan.

4.11.2 Evaluation of aerosol model retrieval

The implementation allows automatic selection of an aerosol model for each retrieval within a scene, based on minimization of the uncertainty. Figure 10 shows retrieval over Beijing for 12/10/2006 of both AOT and aerosol model for a range of possible aerosol models. Retrieval is mainly discriminated by size distribution; here the retrieval indicates larger particle size (classified as *maritime* model) within the high concentration aerosol region, with predominantly the fine particle model (*continental*) retrieved throughout the remainder of the image. The arc of missing values corresponds to dropout pixels within the AATSR scan. The retrieval shows some stability over dense aerosol. The AERONET station is within the zone indicated as *maritime*, and measures an AOT value of 0.85 at 550nm. Here the choice of a *maritime* aerosol model in the Synergy retrieval leads to an AOT value of 0.8, much closer of to the AERONET value than the default choice of *continental*, which gives an estimated AOT of 0.6. While the set of 40 models outlined in Table 8 is available, retrieval time is proportional to the number of allowable aerosol models.

4.11.3 Comparison with AERONET stations

A full comparison is made within the product Validation Report (PVR) of Synergy retrievals compared with Aeronet sun photometer retrievals (Holben et al., 2001), and with the two available single-sensor MERIS algorithms, MERIS L2 (Santer et al., 2007) and IBAER (von Hoyningen-Huene et al., 2006). The dataset is split into scenes including DDV in proximity to the Aeronet sites (20 scenes), and the full set (51 matches).

Figure 14 shows retrieval for DDV scenes. All scatter plots show Aeronet data as common reference (x-axis) and the AOT retrieved with various algorithms as dependent variable (y-axis). The plots show the individual data points (blue circles), the 1:1 line (black solid line), the result of a linear regression analysis in a box and the linear regression fit function as blue solid line. Comparison with AERONET values was undertaken using a fixed aerosol model for all scenes (*continental*).

Over the DDV set (Figure 14), the results show correlation coefficient between AERONET and the

Synergy retrieval of 0.98. The Synergy has mean absolute error (0.04) and bias (<.005) over this dataset. The Synergy retrieval shows very high accuracy for the lower AOTs. At high AOT values, the retrieval is sensitive to choice of aerosol model, and some error is introduced to the Synergy approach by the selection of a single model for testing. Over the full image set including bright targets (Figure 15), the Synergy correlation coefficient is 0.86, with mean absolute error 0.08 and bias -0.02.

4.11.4 Sensitivity to missing sensor data

To evaluate the impact of missing sensor data, for example in areas of the swath where we do not have the SLSTR off-nadir view the retrieval was run over the test dataset to produce three sets of results using (i) only the AATSR retrieval component based on the angular retrieval approach, (ii) using only the MERIS retrieval component based on the spectral retrieval approach, and (iii) retrieval using the full algorithm (MERIS and AATSR data combined). The AATSR-only retrieval therefore corresponds to the same algorithm as used in the Swansea University AATSR retrieval scheme, which has been implemented to produce a successful global product on ESA GPOD.

Over the DDV image set, the results show mean absolute error of 0.09 for either MERIS-only or AATSR-only cases, compared with 0.04 for the Synergy retrieval, and. The correlation coefficient between AERONET and MERIS-only is 0.96, and AATSR-only retrieval is 0.86, and the. The case for all scenes (DDV and bright) shows mean absolute error is 0.12 for AATSR-only and 0.15 for MERIS-only, compared with .08 for Synergy. The correlation coefficient is 0.71 for MERIS-only and 0.78 for AATSR-only retrievals.

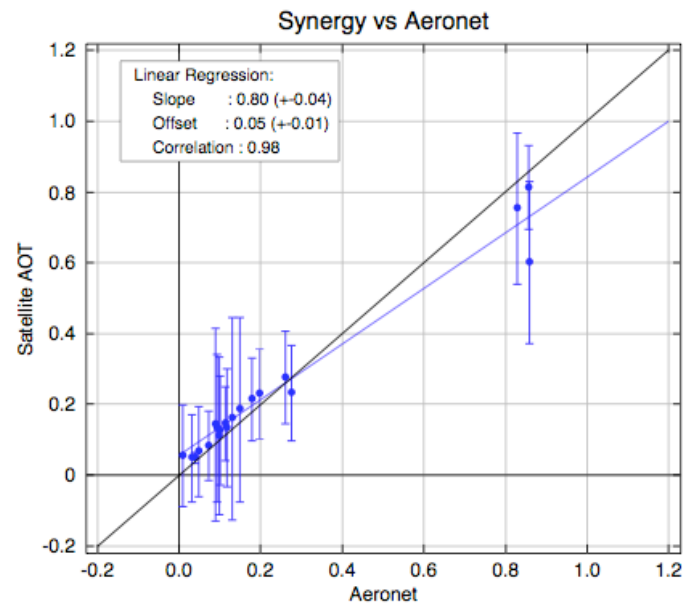


Figure 11. Results of Synergy retrieval compared with AERONET sites (DDV targets only).

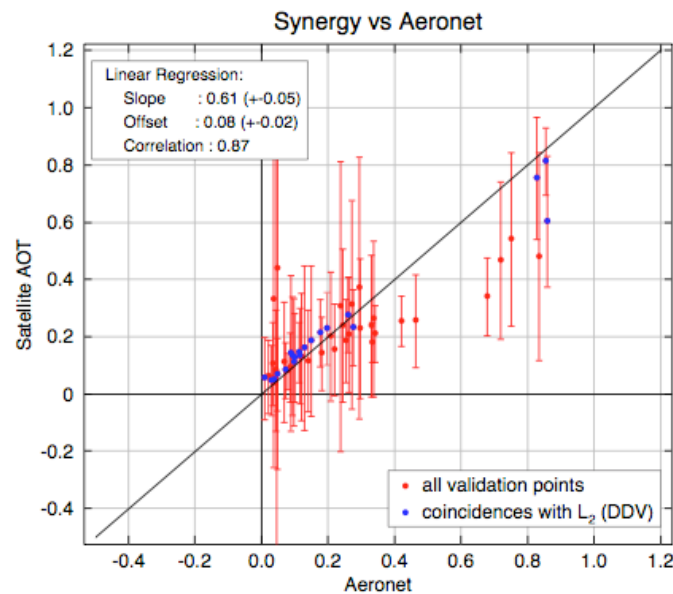


Figure 12. Results of Synergy Retrieval compared with AERONET (full data set), with DDV subset highlighted in blue.

4.12 Summary

The algorithm to estimate aerosol and surface reflectance from TOA OLCI and SLSTR synergy is presented. The main components of this algorithm are (i) radiative transfer modelling of TOA reflectance to generate lookup tables for a range of aerosol optical depths and aerosol model types, (ii) definition of parameterised models of land surface spectral and angular reflectance, (iii) an inversion algorithm to estimate the optimal atmospheric profile, and (iv) atmospheric correction to estimate surface reflectance for MERIS and AATSR channels.

4.12.1 Assumptions and limitations

- The Level 1c product includes column O_3 , water vapour and surface pressure available at tie-points.
- The Level 1c product allows collocation of all wavebands, including SLSTR along-track, at 1km, with accuracy of 0.1km. The L2 algorithm will produce a collocated product on the OLCI grid.
- The algorithm assumes availability of a robust cloud mask – currently we use the union of individual instrument cloud masks, but recommend future work to use ongoing research for cloud classification based on the full synergy information.
- The algorithm gives greatest accuracy for regions where information from all three images (SLSTR backward, SLSTR nadir and OLCI) is available. However the algorithm will also operate for swath regions where either the SLSTR backward is not available, or where OLCI information is unavailable; in these cases a reduced set of constraints is summed in the error function (11).

5 ALGORITHM DESCRIPTION – VGT CONTINUITY

5.1 Theoretical Description

The aim is to allow processing of data from SLSTR and OLCI to provide comparable products to SPOT-VGT, to allow continuity of data delivery for existing user community of SPOT-VGT. The Sentinel-3 instruments differ in angular and spectral sampling to VGT. However, previous research [RD-5] has indicated that by combining information from the SLSTR and OLCI, sufficiently similar products to VGT can be produced. The full specification for the necessary algorithms is given in the reference documents for these studies. Here we define the necessary products and summarise the key points of implementation in the Sentinel-3 processing chain.

SPOT4-VGT was launched in 1998 and continued in 2002 with SPOT5-VEGETATION; the Sentinel-3 mission offers an opportunity for continuity of products, in particular to allow analysis of long time series of land vegetation properties. The products selected for continuity are the P, S1 and S10 products. The P projection is defined at top of atmosphere (TOA), while the S1 and S10 are composite products defined at top of canopy (TOC), i.e. after an atmospheric correction. Both are composite products defined at top of canopy (TOC), i.e. after an atmospheric correction. S1 is defined over a daily time period and S10 over a 10-day (decade) period. Vegetation index maximum value compositing is used to reduce the effects of cloud and atmospheric contamination.

5.2 Algorithm implementation

5.2.1 Overview

The algorithm presented is based closely on the ESA study [RD-5] and ATBD produced [RD-6] to define algorithms for SPOT-VGT continuity. We use as the starting point the co-located TOA L2 product from the SYN branch. There are two deviations. First we use the radiative transfer scheme previously defined for relation of surface reflectance to TOA, adapted for the hyperspectral interpolation and for SPOT-VGT bands. Secondly the retrieved aerosol value from SYN is used to offer an improved surface reflectance for S1 and S10 products. The previous VGT processing uses only a climatology of aerosol varying with latitude, but we recommend the algorithm is also configurable to use this climatology if preferred for continuity.

The processing scheme is outlined in Figure 13. Beginning with the SYN collocated TOA reflectance, there are two stages: (i) spectral mapping to simulate the SPOT-VGT spectral bands at TOA, and (ii) pixel flagging, projection and compositing to generate simulated P, S1 and S10 products.

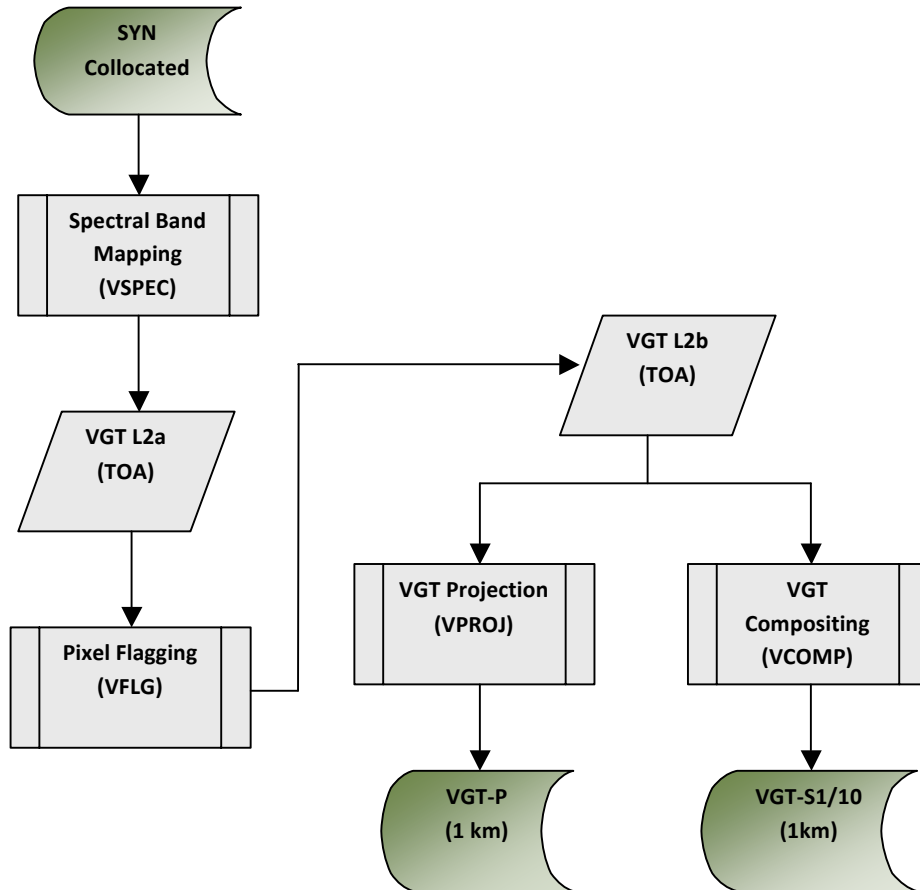


Figure 13. Overview of SPOT-VGT product simulation

Table 10: VEGETATION spectral band specifications and Sentinel-3 bands required for simulation

Channel	Wavelength range (nm)	Band name	OLCI bands required	SLSTR bands required
1	430- 470	B0	2,3	-
2	610 - 680	B2	6-10	-
3	780 - 890	B3	16- 21	-
4	1580 - 1750	MIR	-	5-6

5.2.2 Spectral band mapping procedure

The spectral mapping procedure is summarized in figure 16. The spectral band mapping estimates the 4 broadband VGT-like TOA reflectances, beginning with a simple atmospheric correction of the collocated OLCI and SLSTR data. Simulation requires use of both instruments in order to span the spectral range. Bands from OLCI are used to simulate VGT bands B0, B2 and B3, while SLSTR is used to simulate VGT band MIR (Table 10).

- (1) Beginning with the collocated OLCI/SLSTR product from SYN, we atmospherically correct the nadir data only to produce an image of surface reflectance. This uses equation (6) applied for each pixel, using the LUT already defined for SYN wavebands. For this stage it is not necessary to use accurate AOD, and the climatology value is used (equation (17)) for a standard continental aerosol model, and with the ECMWF column ozone and water vapour. Correction takes place over all pixels, including those flagged as clouds also.
- (2) From this set of OLCI and SLSTR atmospherically corrected reflectance, we use linear interpolation to form a hyperspectral surface reflectance spectrum at 1nm for the range 400-2500 nm. To bracket the VGT wavebands, we need to process the subsets 410-500 nm (B0); 560-780 nm (B2); 700-1000 nm (B3); 1500-1800 nm (MIR)
- (3) We upscale the spectrum within these ranges to TOA using equation (2), based on retrieval of the coefficients by linear interpolation from a LUT as before. Due to the number of wavebands (~900) it is not practical to use the fine resolution in angular sampling for this stage. Instead we use the reduced set of intervals given in Table 11, and a single standard continental aerosol model. We assume the OLCI solar/view geometry for the set of 1nm spectral wavebands defined above. The ECMWF column ozone and water vapour are used, along with the SYN aerosol model and optical thickness.

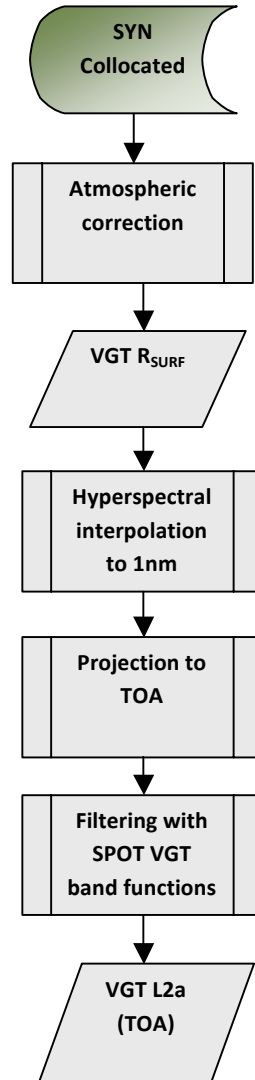


Figure 14. Overview of SPOT-VGT spectral band mapping procedure

- (4) This hyperspectral TOA spectrum is filtered according to the spectral response functions (SRF's) of the VGT bands (B0, B2, B3 and MIR) to obtain simulated reflectance (VGT L2a), using:

$$R_Y^{TOA} = \frac{\int F_0(\lambda) R_Y^{TOA}(\lambda) SRF_Y(\lambda) d\lambda}{\int SRF_Y(\lambda) F_0(\lambda) d\lambda} \quad (17)$$

where F_0 is the exoatmospheric solar irradiance.

Errors due to spectral sampling are reported to be low (~3%) compared to other sources [RD-5].

Table 11: Breakpoints used in the LUT for VGT TOA hyperspectral simulation.

Parameter	Range	Interval	Number of breakpoints
Waveband	410-500 nm 560-780 nm 700-1000 nm 1500-1800 nm	1 nm	914
RAZ	0 - 180°	18°	10
SZA	0 - 70°	Variable depending on Gaussian integration 10° (mean interval)	7
VZA	0 - 55°	Variable depending on Gaussian integration 9° (mean interval)	6
Aerosol properties -AOD at 550 nm	0.0, 0.1, 0.4, 1.0, 2.0, 4.0	0.0, 0.1, 0.4, 1.0, 2.0, 4.0	6
Surface pressure	1030 -800 hPa.	1030, 1000, 900, 800 hPa	4
Water vapour	0, 2, 5 g cm ⁻²	0, 2, 5 g cm ⁻²	3

5.2.3 TOA Processing (VGT P)

The output of the spectral band mapping is TOA reflectance at the 4 VGT channels, on the SYN grid, at 300m. This corresponds directly to the VGT P product reflectance at the four bands. Additional steps required are to add the VGT status flags and to project to Plate-Carrée. The product fields are listed in Table 12.

TOA processing consists of pixel flagging, indicating land, water, cloud cover, ice/snow, and cloud shadows (individual flags are listed in Table 14). The quality flags as well as the land-water mask result from flags present in the L2 SYN products. Detection of clouds, ice/snow and cloud shadows are described in the following paragraphs. For formation of the simulated VGT products we resample to Plate-Carrée at 1km resolution, to conform to continuity of the VGT products.

Table 12: VGT P product pixel data

ID	Description	Type
B0T	TOA reflectance for VGT band B0 (blue)	Float
B2T	TOA reflectance for VGT band B2 (red)	Float
B3T	TOA reflectance for VGT band B3 (NIR)	Float
MIRT	TOA reflectance for VGT band B4 (SWIR)	Float
VZA	View zenith angle	Float
VAA	View azimuth angle	Float
SZA	Solar zenith angle	Float
SAA	Solar azimuth angle	Float
SM	Status flags as in Table 14.	Byte

Table 13: VGT S product pixel data

ID	Description	Type
B0	Surface reflectance composite for VGT band B0 (blue)	Float
B2	Surface reflectance composite for VGT band B2 (red)	Float
B3	Surface reflectance composite for VGT band B3 (NIR)	Float
MIR	Surface reflectance composite for VGT band B4 (SWIR)	Float
VZA	View zenith angle composite	Float
VAA	View azimuth angle composite	Float
SZA	Solar zenith angle composite	Float
SAA	Solar azimuth angle composite	Float
NDVI	Normalised differential vegetation index composite	Float
SM	Status flags as in Table 14.	Byte
TG	Time of observation composite	TBD
Map Info	Information on map projection and grid geometry	Object

Table 14: VGT status flags

Bit	Flag	Value = 0	Value = 1
0	Cloud	Clear or uncertain	Shadow or cloud
1	Cloud	Clear or shadow	Uncertain or cloud
2	Ice/snow	No	Yes
3	Land or water	Water (sea, lakes, etc.)	Land
4	Quality MIR	Poor	Good
5	Quality B3	Poor	Good
6	Quality B2	Poor	Good
7	Quality B0	Poor	Good

5.2.3.1 Detection of clouds

The detection of clouds uses the results of the L2 SYN cloud screening based on union of OLCI and SLSTR cloud flags, which are more elaborate than the threshold-based detection described in [RD-7], and make use of the thermal information and finer spatial resolution not available from the VGT product alone.

5.2.3.2 Detection of ice/snow

The detection of ice/snow uses the results of the OLCI L2 Pixel Classification algorithm, which is carried out in terms of the L2 SYN cloud screening.

5.2.3.3 Detection of cloud shadows

The description of the detection of cloud shadows given in [RD-7] is not adequate enough for deriving an algorithm.

5.2.3.4 VGT Projection

The L2 SYN products are provided with an ortho-geolocation grid defining longitude, latitude, and altitude for each pixel. For the resampling onto the VGT-L2 grid the inverse ortho-geolocation function for the OLCI reference channel is needed.

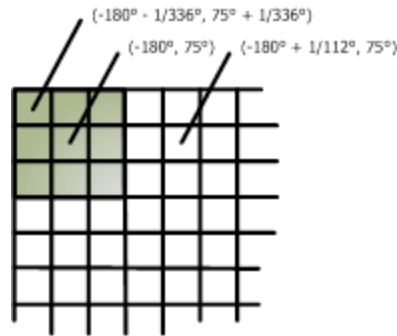


Figure 15: VGT 1 km Plate-Carrée grid cell (green square)

The SPOT VGT Plate-Carrée grid has 112 pixels per degree, which corresponds to an equatorial resolution of about 1 km (Figure 15). The projection and averaging of the values intermediate VGT L2b product results in the VGT-P product. The status flag is set to zero if any of the contributing pixel flags has a zero value. The set of status flags are listed in Table 14.

5.2.3.5 Direct ortho-geolocation

An approximation of the value of the direct ortho-geolocation function at pixel (k, j) can be computed from its sampled representation by using simple interpolation methods. A bilinear or bi-quadratic interpolation method can be used to approximate longitude $\lambda(k, j)$ and latitude $\phi(k, j)$ from the neighbouring samples in the grid.

5.2.3.6 Inverse ortho-geolocation

The computation of the inverse ortho-geolocation of for a pixel, which is located at (λ, ϕ) is an iterative process that makes use of the direct ortho-geolocation approximation.

5.2.4 S1 and S10 Products

5.2.4.1 Atmospheric correction

For the S1 and S10 products the next processing stage is atmospheric correction of the P product data to obtain top-of-canopy (TOC) reflectance. This uses equation (6) applied for each pixel, using a LUT defined for the VGT wavebands. Here we use the same break-point sampling density as for OLCI (Tables 6-7). The atmospheric correction for Sentinel-3 products should use the LUT and aerosol retrieval procedure outlined in chapter 5 of this document. The original SPOT-VGT correction was carried out using a single continental aerosol model and optical thickness given only by an aerosol climatology parameterised by latitude. The aerosol climatology value for optical depth at 550nm is defined by:

$$\tau_{550} = 0.2(\cos(lt) - 0.25) \left(\sin \left(lt + \frac{\pi}{2} \right) \right)^3 + 0.05 \quad (18)$$

The product should be configurable to use this value if preferred for continuity.

5.2.4.2 S1 Products

The S1 products give a single ‘best’ value for TOC reflectance at the four VGT channels, based on those giving the maximum value of a vegetation index. The normalised differential vegetation index NDVI is used, a simple numerical indicator that is widely used to give an indicator of vegetation amount, derived from the VGT channels B3T (NIR) and B2T (red):

$$NDVI = \frac{\rho_{NIR} - \rho_{red}}{\rho_{NIR} + \rho_{red}} \quad (19)$$

While theoretically values in the range -1 to +1 are possible, the NDVI typically gives values between 0.2 and 0.8 for sparsely up to densely vegetated areas. Cloud and ice give values close to zero, and high aerosol loading also reduces the NDVI as it selectively brightens the red wavelength. These products provide data from all spectral bands, the NDVI and auxiliary data on image acquisition parameters. The product format for both S1 and S2 is listed in Table 13.

5.2.4.3 S10 Products

The method and principals for generation of the S3 product are identical to the S1, except that S10 is formed using the maximum value composite over a 10-day period. S1 and S10 can either be generated in parallel, as is the case in CTIV, or alternatively S10 can be generated from S1. The advantage of the former approach is that the same compositing program can be used to generate S1 and S10 [RD-5].

5.3 Assumptions and limitations

The following assumptions are made

- The Level 1c product includes data on O₃, water vapour and pressure available at tie-points.
- The level 1c product allows all bands to be collocated onto a common 300m grid.
- The Level 1c product includes pixel flags indicating: land, water and cloud.

The main limitation is that while the aim is to preserve continuity of product to facilitate change detection over the time series, there are likely to be important artefacts introduced by the differing spatial and spectral sampling characteristics. Temporal sampling is slightly lower, which may result in more cloud and atmospheric effects remaining in the Sentinel-3 S1 and S10 products. For spectral resampling, results of testing on data simulated from MERIS and AATSR showed that depending of the spectral band, an accuracy of 3 to 5% could generally be expected [RD-5]. However large differences between VGT images and those simulated by MERIS/AATSR were reported, due to differences in view geometry and cloud detection.

6 CONCLUSIONS

A synergistic approach, combining the spectral and angular information from the two sensors, offers the potential for improved characterization of aerosol properties and land surface reflectance, and continuity of products from the SPOT-VGT series. Testing on MERIS/AATSR data suggests significant improvement over single sensor formulation. Exploitation of the instrument synergy is an active research area, and further products, e.g. improved cloud screening, ocean aerosol and land biophysical products are likely to be possible and should be considered for future research and implementation.

7 REFERENCES

- Aguirre, M., B. Berruti, J-L. Bezy, M. Drinkwater, F. Heliere, U. Klein, C. Mavrocordatos, P. Silvestrin, B. Greco, J. Benveniste, (2007) Sentinel-3 The Ocean and Medium-Resolution Land Mission for GMES Operational Services, *ESA Bulletin* **131**, 24-29.
- Alton, P.B., North, P. R. J. and Los, S. O. (2007). The impact of diffuse sunlight on canopy light-use efficiency, gross photosynthetic product and net ecosystem exchange in three forest biomes, *Global Change Biology*, **13(4)**, doi:10.1111/j.1365-2486.2006.01316.x.
- Barton, I. J., Zavody, A. M., O'Brien, D. M., Cutten, D. R., Saunders, R. W., & Llewellyn-Jones, D.T. (1989). Theoretical algorithms for satellite-derived sea-surface temperatures. *Journal of Geophysical Research - Oceans*, **94**, 3365 – 3375.
- Bellouin, N., O. Boucher, J. Haywood, and M.S. Reddy, (2005): Global estimation of aerosol direct radiative forcing from satellite measurements, *Science*, **438**, 1138-1141.
- Berthelot, B. and Dedieu, G., Operational method to correct VEGETATION satellite measurements from atmospheric effects. Proceedings IGARSS 2000. *IEEE 2000 International*. 01/02/200002/2000; 2:831-833 vol.2. DOI: 10.1109/IGARSS.2000.861718.
- Bevan, S.L., North, P.R.J., Grey, W.M.F., Los, S.O. and Plummer, S.E. (2009), Impact of atmospheric aerosol from biomass burning on Amazon dry-season drought. *Journal of Geophysical Research*, **114**, D09204, doi:10.1029/2008JD011112.
- Bevan, S.L., North, P.R.J., Los, S.O. and Grey, W.M.F. (2012). A global dataset of atmospheric aerosol optical depth and surface reflectance from AATSR. *Remote Sensing of Environment*, **116**, 119-210.
- Davies, W.H., North, P.R.J., Grey, W.M.F. and Barnsley, M.J. (2010), Improvements in Aerosol Optical Depth Estimation using Multi-angle CHRIS/PROBA Images, *IEEE Transactions on Geoscience and Remote Sensing*, **48(1)**, 18-24.
- Diner, D. J., Asner, G. P., Davies, R., Knyazikhin, Y., Muller, J. P., Nolin, A. W., Pinty, B., Schaaf, C. B., & Stroeve, J. (1999). New directions in Earth observing: scientific applications of multiangle remote sensing. *Bulletin of the American Meteorological Society*, **80** (11), 2209 – 2228.

- Diner, D., J. Martonchik, R. Kahn, B. Pinty, N. Gobron, D. Nelson, and B. Holben, (2005). Using angular and spectral shape similarity constraints to improve MISR aerosol and surface retrievals over land, *Remote Sensing of Environment*, **94**, 155-171.
- Dubovik, O., (2005). Optimization of Numerical Inversion in Photopolarimetric Remote Sensing, in *Photopolarimetry in Remote Sensing, NATO Science Series II: Mathematics, Physics and Chemistry*, Springer Netherlands, ISBN 978-1-4020-2368-2 (Online), 65-106.
- Fell F. and J. Fischer, (2001). Numerical simulation of the light field in the atmosphere-ocean system using the matrix-operator method, *JQSRT*, **69**, 351-388.
- Fischer, J. and Grassl, H. (1984). Radiative transfer in an atmosphere-ocean system: an azimuthally dependent matrix-operator approach, *Appl. Optics* **23**, 1035-1039.
- Fischer and Preusker (2009), Radiative Transfer Model Description Document for ESA AATSR/MERIS Synergy project, available online at <http://www.brockmann-consult.de/beam-wiki/display/SYN/Documents>.
- Flowerdew, R. J., & Haigh, J. D. (1996). Retrieval of aerosol optical thickness over land using the ATSR-2 dual look radiometer. *Geophysical Research Letters*, **23** (4), 351 – 354.
- Govaerts, Y. M., S. Wagner, A. Lattanzio, and P. Watts (2010), Joint retrieval of surface reflectance and aerosol optical depth from MSG/SEVIRI observations with an optimal estimation approach: 1. Theory, *J. Geophys. Res.*, **115**, D02203, doi:10.1029/2009JD011779.
- Grey., W.M.F., North., P.R.J., Los, S.O., and Mitchell, R.M., (2006). Aerosol optical depth and land surface reflectance from multi-angle AATSR measurements: Global validation and inter-sensor comparisons. *IEEE Transactions on Geoscience and Remote Sensing*, **44(8)**, 2184 – 2197.
- Grey., W.M.F, North., P.R.J., and Los, S. (2006b). Computationally efficient method for retrieving aerosol optical depth from ATSR-2 and AATSR data, *App. Optics*, **45(12)**: 2786-2795.
- Guanter, L.; M. Del Carmen González-Sanpedro, J. Moreno, (2007), A method for the atmospheric correction of ENVISAT/MERIS data over land targets, *International Journal of Remote Sensing*, **28(3-4)**, 709-728.
- Hess, M., P. Koepke, and I. Schult, 1998: Optical Properties of Aerosols and Clouds: The Software Package OPAC. *Bull. Amer. Meteor. Soc.*, **79**, 831–844.
- Holben, B., et al. (2001) An emerging ground-based aerosol climatology: Aerosol optical depth from AERONET, *J. Geophys. Res.*, 106(D11), 12067-12097.
- Holzer-Popp, T., Schroedter, M. and Gesell, G. (1999). High-Resolution Aerosol Maps Exploiting the Synergy of ATSR-2 and GOME , *Earth Observation Quarterly* (65): 19-24, ESA Publications Division, ISSN 0256 - 596X.

- Holzer-Popp, T., M. Schroedter-Homscheidt, H. Breitzkreuz, L. Klüser, D. Martynenko, (2008). Synergetic aerosol retrieval from SCIAMACHY and AATSR onboard ENVISAT, *Atmospheric Chemistry and Physics Discussions*, **8**, 1-49.
- Hsu, N. C., S.-C. Tsay, M. D. King, and J. R. Herman, (2004) Aerosol properties over bright-reflecting source regions, *IEEE Transactions on Geoscience and Remote Sensing*, **42**(3), 557– 569.
- Jacquemoud, S., & Baret, F. (1990). PROSPECT: a model of leaf optical properties spectra, *Remote Sensing of Environment*, **34**, 75-9.
- Jeong, M.-J., and N. C. Hsu (2008), Retrievals of aerosol single-scattering albedo and effective aerosol layer height for biomass-burning smoke: Synergy derived from “A-Train” sensors, *Geophys. Res. Lett.*, **35**, L24801, doi:10.1029/2008GL036279.
- Kaufman Y. J. and Sendra, C. (1988). Algorithm for automatic corrections to visible and near IR satellite imagery, *Int. J. Remote Sensing*, **9**, 1357-1381.
- Kaufman, Y.J. and Tanré D. (1992), Atmospherically resistant vegetation index (ARVI) for EOS-MODIS, *IEEE Transactions on Geoscience and Remote Sensing*, **30**, 261-270.
- Kokhanovsky, A.A., F.-M. Breon, A. Cacciari, E. Carboni, D. Diner, W. Di Nicolantonio, R.G. Grainger, W.M.F.Grey, R. Holler, K.-H. Lee, P.R.J. North, A. Sayer, G. Thomas, W. von Hoyningen-Huene, (2007). Aerosol remote sensing over land: satellite retrievals using different algorithms and instruments. *Atmospheric Research*, **85**, 372-394, doi:10.1016/j.atmosres.2007.02.008.
- Kotchenova, S.Y., Vermote, E.F., Matarrese, R. and Klemm, F.J. (2006), Validation of a vector version of the 6S radiative transfer code for atmospheric correction of satellite data. Part I: path radiance. *Applied Optics*. 10/2006; **45**(26):6762-74.
- Leroy M., Deuze J.L., Bréon F.M., Hautecoeur O., Herman M., Buriez J.C., Tanre D., Bouffies S., Chazette P., and Roujean J.L., (1997). Retrieval of atmospheric properties and surface bidirectional reflectances over the land from POLDER. *Journal of Geophysical Research* **102** (D14), 17023-17037.
- Levy, R.C., Remer, L., Mattoo, S., Vermote, E. and Kaufman, Y.J. (2007), Second-generation algorithm for retrieving aerosol properties over land from MODIS spectral reflectance. *J. Geophys. Res.*, **112**, D13211, doi:10.1029/2006JD007811.
- Lyapustin, A. and Wang, Y., (2009). The time series technique for aerosol retrievals over land from MODIS, in *Satellite Aerosol Remote Sensing Over Land*, A. A. Kokhanovsky and G. DeLeeuw, Eds. Heidelberg: Springer Praxis Books, ISBN: 978-3-540-69396-3, pp. 69–99.
- Mackay, G., M.D. Stevens, and J.A. Clark (1998). An atmospheric correction procedure for the ATSR-2 visible and near-infrared land surface data. *Int. J. Remote Sensing* **19**, 2949- 2968.

- Martonchik, J.V., D.J. Diner, R. A. Kahn, T.P. Ackerman, M. M. Verstraete, B. Pinty, and H.R. Gordon,(1998). Techniques for retrieval of aerosol properties over land and ocean using multiangle imagery. *IEEE Trans. Geosci. Rem. Sens.* **36**, 1212-1227
- McGill, M.J., L. Li, W.D. Hart, G.M. Heymsfield, D.L. Hlavka, P.E. Racette, L. Tian, M.A. Vaughan, and D.M. Winker, (2004). Combined lidar-radar remote sensing: initial results from CRYSTAL-FACE, *Journal of Geophysical Research*, 109, doi: 10.1029/2003JD004030.
- Mishchenko M.I., I.V. Geogdzhayev, B. Cairns, B.M. Carlson, J. Chowdhary, A.A. Lacis, L. Liu, W.B. Rossow, L.D. Travis, (2007). Past, present, and future of global aerosol climatologies derived from satellite observations: A perspective, *Journal Of Quantitative Spectroscopy & Radiative Transfer* **106 (1-3)**, 325-347.
- North, P.R.J. (1996), Three-dimensional forest light interaction model using a Monte Carlo method, *IEEE Transactions on Geoscience and Remote Sensing*, **34(5)**, 946-956.
- North, P.R.J., Briggs, S.A., Plummer, S.E. and Settle, J.J., (1999). Retrieval of land surface bidirectional reflectance and aerosol opacity from ATSR-2 multi-angle imagery, *IEEE Transactions on Geoscience and Remote Sensing*, **37(1)**, 526-537.
- North, P.R.J. (2002a). Estimation of fAPAR, LAI and vegetation fractional cover from ATSR-2 imagery. *Remote Sensing of Environment* **80**:114–121.
- North, P. R. J. (2002b). Estimation of aerosol opacity and land surface bidirectional reflectance from ATSR-2 dual-angle imagery: Operational method and validation, *J. Geophys. Res.*, **107**, doi:10.1029/2000JD000,207.
- North, P.R.J., Brockmann , C., Fischer, J., Gomez-Chova, L., Grey, W., Hecklel A., Moreno, J., Preusker, R. and Regner, P. (2008). MERIS/AATSR synergy algorithms for cloud screening, aerosol retrieval and atmospheric correction. *In Proc. 2nd MERIS/AATSR User Workshop, ESRIN, Frascati, 22- 26 September 2008*. (CD-ROM), ESA SP-666, ESA Publications Division, European Space Agency, Noordwijk, The Netherlands.
- Press, W.H., S.A. Teukolsky, W.T. Vetterling, and B.P. Flannery, (1992). *Numerical Recipes in C, The Art of Scientific Computing (Second Edition)*. Cambridge: Cambridge University Press.
- Prieto-Blanco, A., North, P.R.J., Fox, N. and Barnsley, M.J. (2009). Satellite-driven modelling of Net Primary Productivity (NPP): Theoretical analysis. *Remote Sensing of Environment* **113(1)**, 137-14.
- Rahman, H., and G. Dedieu (1994). SMAC : A simplified method for the atmospheric correction of satellite measurements in the solar spectrum. *International Journal of Remote Sensing*, **15(1)**, 123-143.
- Rathke, C and Fischer, J, (2002). Efficient parameterization of the infrared effective beam emissivity of semitransparent atmospheric layers, *J. Geophys. Res.*, **107** (D4), doi:10.1029/2001JD000596.

- Remer, L. Y. Kaufman, D. Tanre, S. Mattoo, D. Chu, J. Martins, R.-R. Li, C. Ichoku, R. Levy, R. Kleidman, T. Eck, E. Vermote, and B. Holben, (2005). The MODIS Aerosol Algorithm, Products and Validation, *Journal of the Atmospheric Sciences*, **62**, 947-973.
- Rosenfeld, D., Y. Rudich, R. Lahav, (2001). Desert dust suppressing precipitation: A possible desertification feedback loop, *Proceedings of the National Academy of Sciences*, **98**, 11, 5975-5980, doi:10.1073/pnas.101122798.
- Saint, G., (1994). "VEGETATION" onboard SPOT 4, Products Specifications, Version 2, 18 May 1994.
- Santer, R., V. Carrère, P. Dubuisson and J.C. Roger (1999), Atmospheric corrections over land for MERIS, *Int. J. Remote Sensing*, **20** (9), 1819-1840.
- Santer, R., D. Ramon, J. Vidot, E. Dilligeard, (2007). A surface reflectance model for aerosol remote sensing over land, *International Journal of Remote Sensing*, **28(3-4)**, 737-760.
- Santer, R. (2009): MERIS L2 ATBD 2.15, http://envisat.esa.int/instruments/meris/atbd/atbd_2_15.pdf
- Smith, D., Poulsen, C. and Latter, B (2008), Calibration Status of AATSR and MERIS Reflectance Channels, *In Proc. 2nd MERIS/AATSR User Workshop, ESRIN, Frascati, 22- 26 September 2008*. (CD-ROM), ESA SP-666, ESA Publications Division, European Space Agency, Noordwijk, The Netherlands.
- Solomon, S., et al., (2007). "Technical Summary: The Physical Science Basis. Contribution of Working Group I to the Fourth Assessment Report of the Intergovernmental Panel on Climate Change," in *Climate Change 2007*, S. Solomon, D. Qin, M. Manning, Z. Chen, M. Marquis, K. B. Averyt, M. Tignor, and H. L. Miller, Eds. Cambridge, United Kingdom and New York, NY, USA: Cambridge University Press.
- Thomas, G.E., E. Carboni, A.M. Sayer, C.A. Poulsen, R. Siddans, R.G. Grainger (2009), Oxford-RAL Aerosol and Cloud (ORAC): aerosol retrievals from satellite radiometers, in *Satellite Aerosol Remote Sensing Over Land*, A. A. Kokhanovsky and G. de Leeuw (eds.), Springer, 2009.
- Twomey, S.A. (1974). Pollution and the planetary albedo, *Atmospheric Environment*, **8**, 1251-56.
- Veefkind, J. P., de Leeuw, G., Durkee, P. A., Russell, P. B., Hobbs, P. V., & Livingston, J. M. (1999). Aerosol optical depth retrieval using ATSR-2 and AVHRR data during TARFOX. *Journal of Geophysical Research - Atmospheres*, **104** (D2), 2253 – 2260.
- Veefkind J.P., G. de Leeuw, P. Stammes, R.B.A. Koelemeijer, (2000). Regional distribution of aerosol over land, derived from ATSR-2 and GOME, *Remote Sensing of Environment*, **74** (3), 377-386.
- Vermote E.F., D. Tanré, J.L. Deuze, M. Herman, J.J. Morcrette, (1997): Second Simulation of the Satellite Signal in the Solar Spectrum, 6S: An overview, *IEEE Transactions on Geoscience and Remote Sensing*, **35(3)**, 675-686.

Vidot, J., Santer, R., and Aznay, O. (2008) Evaluation of the MERIS aerosol product over land with AERONET, *Atmos. Chem. Phys.*, 8, 7603-7617.

von Hoyningen-Huene W., Freitag M., and Burrows, J.B. (2003), Retrieval of aerosol optical thickness over land surfaces from top-of-atmosphere radiance, *Journal of Geophysical Research*, **108 (D9)**: Art. No. 4260.

von Hoyningen-Huene, W. et al. (2006). Simultaneous determination of aerosol and surface characteristics from top-of-atmosphere reflectance using MERIS on board of Envisat, *Advances in Space Research*, **37**, 2172-2177.

Von Hoyningen-Huene, W., et al.: IBAER ATBD, http://www.brockmann-consult.de/beam/software/plugins/baer-1.0.0/BAER_ATBD_NOV-3160-NT-2703_v2.0.pdf